

Physical properties of B-type asteroids from WISE data

V. Alí-Lagoa^{1,2}, J. de León³, J. Licandro^{1,2}, M. Delbó⁴, H. Campins⁵,
N. Pinilla-Alonso^{6,7} and M. S. Kelley⁸

¹ Instituto de Astrofísica de Canarias (IAC), c/ Vía Láctea s/n, 38205, La Laguna, Tenerife, Spain
e-mail: vali@iac.es

² Departamento de Astrofísica, Universidad de La Laguna. 38206, La Laguna, Tenerife, Spain

³ Departamento de Edafología y Geología, Universidad de La Laguna. 38206, La Laguna, Tenerife, Spain

⁴ UNS-CNRS-Observatoire de la Côte d'Azur, B.P. 4229, 06304 Nice Cedex 4, France

⁵ Physics Department, University of Central Florida, P. O. Box 162385, Orlando, FL 32816.2385, USA

⁶ Instituto de Astrofísica de Andalucía (IAA), Granada, Spain

⁷ Department of Earth and Planetary Sciences, University of Tennessee, 1412 Circle Dr, Knoxville TN 37996-1410

⁸ Department of Astronomy, University of Maryland, College Park, MD 20472-2421, USA

Received 31 October 2012; accepted 19 March 2013 (v1)

ABSTRACT

Aims. Our aim is to obtain more information about the physical nature of B-type asteroids and extend on the previous work by studying their physical properties derived from fitting an asteroid thermal model to their NASA's Wide-field Infrared Survey Explorer (WISE) data. We also examine the Pallas collisional family, a B-type family with a moderately high albedo in contrast to the large majority of B-types.

Methods. We apply a combination of the Near-Earth Asteroid Thermal Model and a model of the reflected sunlight to WISE asteroid data in order to derive up to four parameters: effective diameter (D), the so-called infrared beaming parameter (η), ratio of infrared to visible albedo ($R_p = p_{IR}/p_V$) and visible geometric albedo (p_V).

Results. We obtained the effective diameter, geometric visible albedo, infrared-to-visible albedo ratio and beaming parameter for ≥ 100 B-types asteroids and plotted the value distributions of p_V , R_p and η ($\bar{p}_V = 0.07 \pm 0.03$, $\bar{R}_p = 1.0 \pm 0.2$, and $\bar{\eta} = 1.0 \pm 0.1$). By combining the IR and visible albedos with $2.5 \mu\text{m}$ reflectances from the literature we obtained the ratio of reflectances at 3.4 and $2.5 \mu\text{m}$, from which we found statistically significant indications that the presence of a $3\text{-}\mu\text{m}$ absorption band related to water may be commonplace among the B-types. Finally, the Pallas collisional family members studied (~ 50 objects) present moderately high values of p_V ($\bar{p}_V = 0.14 \pm 0.05$), significantly higher than the average albedo of B-types. In addition, this family presents the lowest and most homogeneously distributed R_p -values of our whole sample, which shows that this group is clearly different from the rest of B-types, likely because its mem-

bers are pieces likely originating from the same region of (2) Pallas, a particularly high-albedo B-type asteroid.

Key words. Minor planets, asteroids: general – Surveys – Infrared: planetary systems

1. Introduction

The study of asteroids is important to gain knowledge about the origin and evolution of our planetary system. Asteroids are relics of the Solar System's formation and the building blocks of the terrestrial planets. Primitive asteroids, i.e. those belonging to the so-called spectroscopic C-complex and having in general visible geometric albedo $p_V \lesssim 0.1$ and featureless, flat visible spectra, are particularly relevant in this context. Thought to have formed further away from the sun than the other asteroid classes, primitive asteroids have experienced less heating and alteration processes and have a more pristine composition, potentially preserving crucial information about the early Solar System. In addition, primitive asteroids play an important role in current exobiological scenarios as they delivered complex organic molecules to the early Earth. This organic matter is prerequisite for the synthesis of pre-biotic biochemical compounds that would subsequently lead to the emergence of life (Maurette 2006, and references therein). For these and other reasons, upcoming sample return space missions have selected primitive asteroids as primary targets: NASA's OSIRIS-Rex (Campins et al. 2010b; Lauretta et al. 2010), ESA's Marco Polo-R (Barucci et al. 2012; de León et al. 2011); and JAXA's Hayabusa-2¹.

The taxonomic classification of primitive asteroids has been traditionally based on their low visible albedo ($\lesssim 0.08$ – 0.1), relatively flat or slightly blue visible spectra and the weak or no absorption features thereof (for a detailed review, see Clark et al. 2010). Several primitive classes were defined in Tholen's taxonomy, e.g. B, C, F, G, D and P (Tholen 1984, 1989). Bus' feature-based classification, independent of the albedo, merged some of these and defined new primitive taxons that were extended with minor changes into the Bus-DeMeo taxonomy (Bus & Binzel 2002; DeMeo et al. 2009).

B-types are of particular interest among the primitive asteroids for a number of reasons: (i) there is as yet no compelling explanation for their defining feature, i.e. their slightly blue spectral slope in the visible range; (ii) B-type asteroids constitute the only primitive class that presents a wide range of spectral slopes in the 0.8 – $2.5 \mu\text{m}$ near-infrared region, from negative to positive, in the 0.8 – $2.5 \mu\text{m}$ near-infrared region (de León et al. 2012); (iii) the few B-types studied present the $3\text{-}\mu\text{m}$ absorption feature related to hydrated minerals; (iv) water ice has been detected on the surface of (24) Themis (Campins et al. 2010a; Rivkin & Emery 2010); (v) the majority of asteroids that have been observed to display cometary-like activity are B-types (Licandro et al. 2012, and references therein); (vi) the target of NASA OSIRIS-Rex mission, 2006 RQ₃₆, is a B-type asteroid.

B-type asteroids have been widely related to carbonaceous chondrites, composed of carbonaceous minerals and phyllosilicates, in terms of their generally low albedo and broad spectral properties (Gaffey et al. 1989; Vilas & Gaffey 1989; Vilas et al. 1994). More recently, de León et al. (2012) examined visible to near-infrared (VNIR) spectra of a sample of 45 B-types and found that the characteristic negative spectral slope in visible wavelengths diverges into a continuum of gradually varying spectral slopes in the 0.8 – $2.5 \mu\text{m}$ (NIR) range, from a monotonic negative (blue)

¹ <http://www.jspec.jaxa.jp/e/activity/hayabusa2.html>

slope to a positive (red) slope. de León et al. (2012) classified their spectra into six “average spectra” or “centroids” representative of the whole sample by means of statistical clustering analysis (Marzo et al. 2009). These centroids were compared against meteorite spectra from the RELAB database (Pieters & Hiroi 2004). The best meteorite analogues found for the six “clusters” were all carbonaceous chondrites with a gradual change in their degree of hydration, from aqueously altered CM2 chondrites for the reddest cluster, to the heated/thermally metamorphosed CK4 chondrites for the bluest one.

This work is an extension of the results obtained by de León et al. (2012), which are part of an ongoing programme devoted to improving our knowledge of B-types. Our aim here is to study the physical properties of B-type asteroids that can be derived by fitting a thermal model to their NASA’s Wide-field Infrared Explorer (WISE) observations, i.e. effective diameter, beaming parameter and p_{IR}/p_V , where p_{IR} is the albedo at 3.4–4.6 μm as defined in Mainzer et al. (2011b). We closely follow the methodology of Mainzer et al. (2011b), though with a number of differences, as described in Sects. 2 and 3.

Mainzer et al. (2011c) studied all groups of spectrophotometrically classified asteroids in the Tholen, Bus and Bus-DeMeo taxonomies observed by WISE, including B-types. Those authors present visible and NIR geometric albedo distributions and median values of B-types and conclude that, in spite of having analogously low albedos, B-, C-, D- and T-type asteroids can be discriminated from their values of NIR reflectance. In particular, Mainzer et al. (2011c) point out that B-types have a lower p_{IR}/p_V ratio than C-types and attribute this to their blue VNIR slopes likely extending out to 3–4 μm . Our definition of B-type asteroid in this work is different: following Clark et al. (2010) and de León et al. (2012), we consider all objects that have a flat to slightly blue spectral slope in the visible range, i.e. any object that has ever been classified as a B-type, including Tholen’s F-types and ambiguous designations. This criterion produces a total of 162 asteroids classified as B-types.

We also study the collisional family of (2) Pallas (hereafter PCF and Pallas, respectively). The PCF is interesting for the following reasons: (i) it is a B-type family, given that Pallas and the very few family members that have been taxonomically classified are B-types (Gil-Hutton 2006; de León et al. 2010), and the five members studied in de León et al. (2012) were spectrally related to carbonaceous chondrites, which establishes their primitive nature; (ii) the average values of geometric albedo of members of the family calculated by Masiero et al. (2011) are roughly 0.15 (see their Fig. 19), significantly greater than expected for primitive bodies (< 0.1), though no explicit comment is made by these authors on this intriguing result; (iii) the Near-Earth asteroid (3200) Phaethon, an activated asteroid parent of the Geminid meteor shower, likely originated in the Pallas family (de León et al. 2010); (iv) this family is well isolated in (proper) element space, thus the potential identification of interlopers as members is greatly reduced.

The paper is organised as follows. In Sect. 2, we briefly describe the WISE data set and our selection criteria. The thermal modelling of the data is explained in detail in Appendix A, whereas Sect. 3 includes relevant comments on the very few differences introduced in this work. In Appendix B our parameter determinations are compared to those by Masiero et al. (2011). We present our results in Sect. 4, a discussion of the implications of this work is put forward in Sect. 5, and our conclusions are enumerated in Sect. 6.

2. Data

A general introduction to WISE can be found in Wright et al. (2010) and references therein. Of particular interest to Solar System science is the NEOWISE project. This acronym collectively refers to two enhancements to the WISE data processing system that were designed to allow detection and archiving of Solar System objects (for details, see Mainzer et al. 2011a).

WISE used four broad-band filters with approximate isophotal wavelengths at 3.4, 4.6, 12 and 22 μm , referred to as W1, W2, W3 and W4, respectively (Wright et al. 2010). The WISE All-Sky Single Exposure L1b Working Database, published in April 2012 and available via the IRSA/IPAC archive², includes the corresponding magnitudes and uncertainties in the Vega system as well as quality and contamination and confusion flags that enable us to reject defective data (Cutri et al. 2012).

We follow a combination of criteria found in Mainzer et al. (2011b,c); Masiero et al. (2011) and Grav et al. (2012) in order to ensure the reliability of the data. We implement the correction to the red and blue calibrator discrepancy in W3 and W4; we use a cone search radius of 0.3'' centred on the MPC ephemeris of the object in our queries; all artifact flags other than p, P and 0 and quality flags other than A, B and C are rejected; we require the modified Julian date to be within 4 seconds of the time specified by the MPC and split groups of epochs separated more than three days (see the end of this section); we ensure that the data is not contaminated by inertial sources by removing those points that return a positive match from the WISE Source Catalog within 6''; finally, all remaining observations in a given band are rejected if they are fewer than 40% of the data in the band with the maximum number of detections.

On the other hand, we do not use data saturated to any extent. The onset of saturation is reported to correspond to magnitudes $M_{W1} < 6$, $M_{W2} < 6$, $M_{W3} < 4$, $M_{W4} < 3$ (Cutri et al. 2012). We found that enlarging the error bar of partially saturated data to 0.2 magnitudes (which translates into a relative error of 20% in fluxes) renders the corresponding band to play no effective role in the thermal model fit by not contributing significantly to the χ^2 .

The application of the above criteria results in a sample of 111 B-type Main-Belt objects with WISE observations usable for our purposes. Some asteroids have been observed by WISE in more than one uninterrupted group of epochs with different observation geometries. We also model separately such groups of observations if they are more than three days apart (see Appendix A and Mainzer et al. 2011b). Consequently, we have a larger set of parameter determinations than asteroids in the sample.

3. Thermal modelling

The modelling of WISE asteroid data implemented in this work closely follows Mainzer et al. (2011b,c); Masiero et al. (2011) and is based on the Near-Earth Asteroid Thermal model (NEATM, Harris 1998) and the IAU phase curve correction to the visible magnitude (Bowell et al. 1989). For the sake of reproducibility, we include a detailed account of our procedure in Appendix A and enumerate the few differences with respect to Masiero et al. and Mainzer et al. below.

The number of parameters we can fit for each object depends upon how many and which WISE bands are present in its data set. Parameter default values are chosen based on the peak of

² <http://irsa.ipac.caltech.edu/Missions/wise.html>

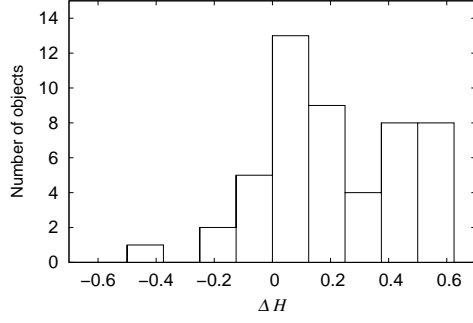


Fig. 1. Differences in absolute magnitude values between those used by Masiero et al. (2011), H_M , and the most updated ones (as of May 2012) used in this paper, H_U . Note that the cases verifying $\Delta H = 0$ do not contribute to this histogram.

their respective fitted value distributions of Main Belt Asteroids presented in Masiero et al. (2011). Whenever there is one single or no thermal band available (W2, W3 or W4) we assume $\eta = 1.0$; R_p is fixed to 1.5 unless we have at least 50% contribution of reflected sunlight in W1 data. The last criterion is based on the consistency of our parameter determinations for objects with double detections³. Namely, both groups of observations of asteroids (1076) and (2446) have > 50% sunlight and their R_p values are consistent within the errorbar. On the other hand, (3579) has non-compatible R_p determination from W1 data with >70% and $\sim 25\%$ reflected sunlight, respectively. We thus reject three R_p values belonging to asteroids (288), (1493) and (3579).

These considerations allow asteroid size to be fitted in all cases and, by means of the relation

$$p_V = \left(1329 \text{ [km]} \frac{10^{-H/5}}{D \text{ [km]}} \right)^2, \quad (1)$$

the geometric visible albedo can be computed. In contrast, W1 and W2 data are more often rejected based on the data requirements (see Sect. 2) than the purely thermal bands and one will usually be able to obtain fewer R_p determinations than η or indeed D .

It is important to point out that we do not use physical data previously determined by direct measurements such as radar diameters or albedos to constrain our fits, i.e. we limit ourselves to using radiometrically derived sizes. This will introduce variations on the parameter determinations of some individual asteroids –specially the largest ones since it is more likely that more direct measurements have been performed– as compared to Masiero et al. (2011), but should not affect the result of statistical analyses if the populations studied consist of a significant number of objects. In Appendix B we show that, given the same input values of H , our best-fit parameter values are consistent within the errorbars, though we find that our R_p determinations are systematically lower by $\sim 10\%$. On the other hand, the update of $\sim 45\%$ of the MPC H -values in our sample does change the values of p_V (see Eq. 1) and R_p . As shown in Fig. 1, the updates tend to be toward greater values of H , which will result in lower p_V and greater values of R_p than those of Masiero et al. (2011). For more details, see Appendix B.

³ This criterion may not be of general applicability and has only been checked for objects in our B-type sample.

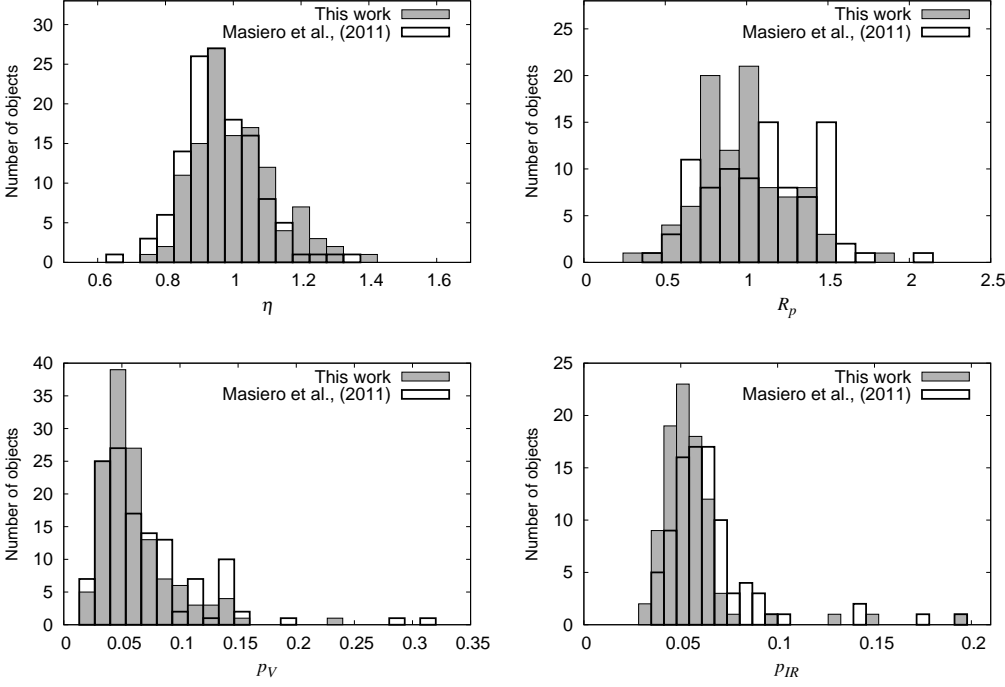


Fig. 2. Histograms of value distributions obtained for the B-type asteroids observed by WISE: η (top left), p_V (bottom left), R_p (top right), and p_{IR} (bottom right). The corresponding histograms using the results from Masiero et al. (2011) are overlotted.

4. Results

4.1. Value distributions of η , p_V and R_p

The distributions of η , p_V , R_p and p_{IR} obtained for the B-types are shown in Fig. 2 (the complete set of parameters determinations is given in Table 1). For comparison, we overlotted the corresponding histograms with best-fit parameter values from Masiero et al. (2011) (see Appendix B for a detailed comparison). The parameter median and mean values and standard deviations of this work, as well as the number of parameter determinations obtained in each case (N), are presented in Table 2. Note that p_V and p_{IR} are not fitted, but computed. The former is obtained from Eq. 1 with the best-fit value of D as input, whereas $p_{IR} = R_p p_V$. These results are consistent with previous work by Mainzer et al. (2011c): if we take the weighted mean of median p_V - and R_p -values corresponding to their Tholen, Bus and Bus-DeMeo B-types and Tholen F-types we obtain the same median values.

We find a η -value distribution centered at unity, consistent with the average value obtained for the whole Main Belt (Masiero et al. 2011). The broad and asymmetrical p_V distribution extends to $p_V > 0.1$. The R_p distribution is also broad, whereas the values of p_{IR} are more compactly distributed around the mean.

4.2. Albedo ratio

Figure 3 shows a plot of R_p versus p_V . Similar plots including all taxonomic classes in different classification schemes are presented in Figs. 14 and 15 by Mainzer et al. (2011c) to show how

Table 2. Median and mean values and standard deviations of η , R_p , p_V and p_{IR} derived for the B-type asteroids observed by WISE.

Parameter	Median	Mean	σ	N
η	1.0	1.0	0.1	116
R_p	1.0	1.0	0.2	88
p_V	0.06	0.07	0.03	132
p_{IR}	0.06	0.06	0.01	88

clearly different taxons may be distinguished. Here we concentrate on the $p_V < 0.18$ range, with all B-types with WISE data for which R_p -values could be derived are plotted in black circles (see Table 2); we also include all main belt asteroids taken from Table 1 of Masiero et al. (2011) (grey empty circles). The cloud of points exhibits a characteristic “waning-moon” shape, with no points in either the high- p_V , high- R_p or low- p_V , low- R_p regions of the plot. Mainzer et al. caution that, while WISE is essentially unbiased against p_V , spectroscopic surveys conducted to create the classification schemes are inherently biased against small, low- p_V objects; in addition, the computation of R_p from WISE data requires sufficient reflected sunlight contribution in bands W1 and W2, which will tend to exclude objects with low enough values of p_V and R_p . This could explain the lack of points in the lower left part of the plot. However, these biases cannot be solely responsible for this characteristic shape since other taxonomic classes with higher values of p_V and R_p also cluster similarly. Furthermore, if we plot all main belt objects irrespective of whether they have a taxonomic classification or not, distinct clouds of points with the same shape become apparent. Thus, we emphasize that because of their characteristic p_V - and p_{IR} -value distributions, there are no high- R_p objects among the high- p_V B-type asteroids.

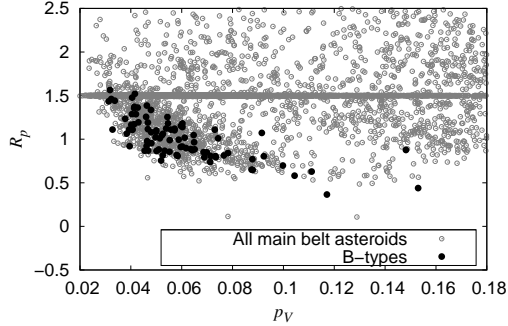


Fig. 3. Albedo ratio versus visible geometric albedo. The 20% errorbars in p_V and R_p are not shown to facilitate visualisation. B-types observed by WISE are plotted in black circles; all main belt objects featured in Table 1 of Masiero et al. (2011) are in empty grey circles. The horizontal line is an artificial feature corresponding to objects with the default fixed value of $R_p=1.5$.

We have also analysed the R_p -values of the sample of 45 B-types studied by de León et al. (2012) separately. The spectra of these asteroids were classified into six “average spectra” or “centroids” referred to as G1, G2, ... G6 (see Sect. 1). These show a progressive decrease in spectral gradient in the NIR interval (0.8–2.5 μm), ranging from a positive (red) slope for G1 to a negative (blue) slope for G6. In Fig. 4, we plot R_p versus p_V labelling the objects in the different centroids

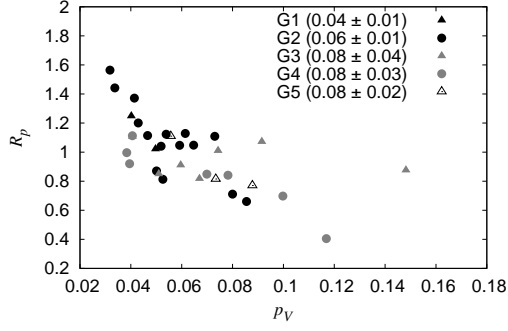


Fig. 4. R_p vs. p_V for the asteroids in de León et al. (2012) distinguishing the clusters to which they belong. Within parentheses, the average p_V of each cluster is shown. On average, p_V increases from G1 to G3, keeping the same value from G3 to G5.

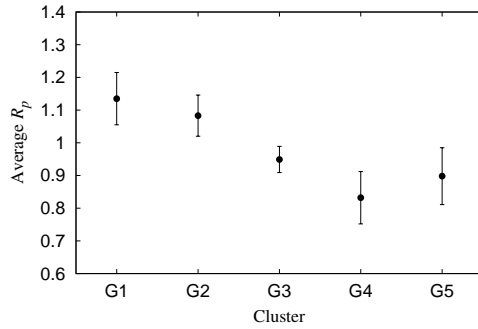


Fig. 5. Average values of R_p for each cluster defined by de León et al. (2012). In terms of spectral slope up to $2.5 \mu\text{m}$, cluster G5 is the bluest, whereas G1 is the reddest. Note: the errorbar is the standard error of the mean.

G1, ... G5. Note that cluster G6 is not included since it is composed only of one member, (3200) Phaethon, which did not have enough WISE observations to perform a reliable fit. The average values of p_V for each cluster increases from G1 to G3, retaining the same value from G3 to G5. This might suggest an inverse correlation between the cluster NIR slope and p_V , though the small number of objects per cluster with WISE observations (2 objects in G1, 12 in G2, 6 in G3, 5 in G4, and 3 in G5) prevents us from establishing a firm conclusion.

In Fig. 5, the average R_p -value is plotted for the different clusters. This figure suggests a correlation between the average R_p and the NIR slope of the relative reflectance of the clusters: objects with higher R_p belong (on average) to clusters with higher NIR spectral slope in the $\sim 1.0\text{--}2.5 \mu\text{m}$ range (see also Fig. 5 of de León et al. 2012). This indicates that the reflectivity at $3.4 \mu\text{m}$ tends to continue the trend observed at shorter IR wavelengths, as hypothesized by Mainzer et al. (2011c).

The W1 band pass spans the 2.8 to $3.8 \mu\text{m}$ range (Wright et al. 2010); therefore, the values of R_p may also be diagnostic of the presence of the $3\text{-}\mu\text{m}$ absorption feature attributed to hydrated minerals or water-ice detected on many asteroids (Rivkin et al. 2000; Gaffey et al. 2002; Campins et al. 2010b; Rivkin & Emery 2010; Licandro et al. 2011). Mainzer et al. (2011c) ruled out the possibility of detecting the hydration band from WISE data based on the fact that the average R_p for a sample of 7 M-types with positive detections of the band (Rivkin et al. 2000) cannot be distinguished from that corresponding to other 33 M-types. However, this test might not be meaningful

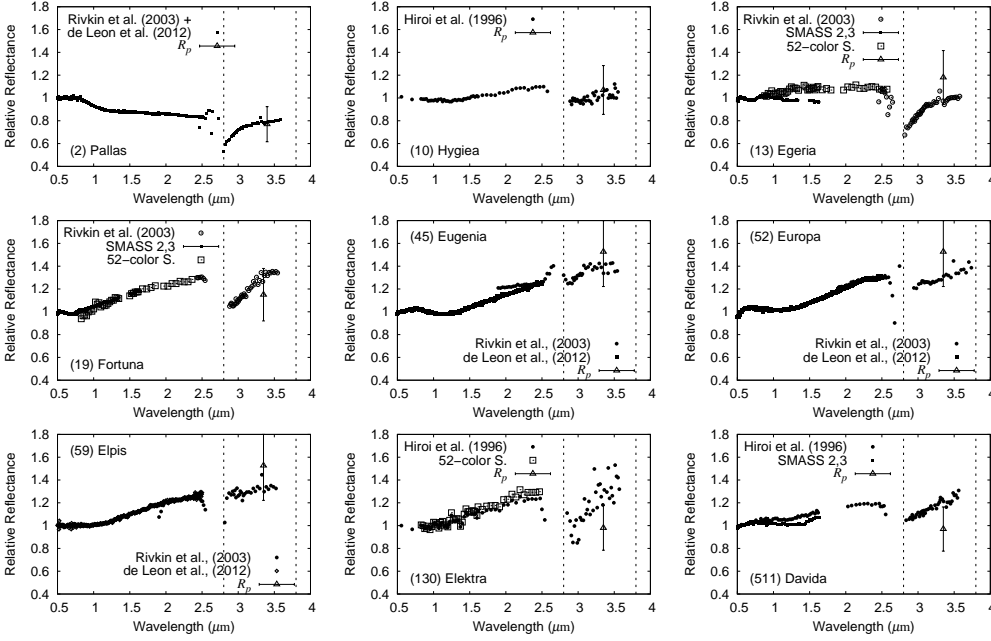


Fig. 6. Assembled spectra of the control objects chosen to study the reflectivity at $3.4 \mu\text{m}$ derived from WISE data as diagnostic of the presence of the $3\text{-}\mu\text{m}$ feature. The dashed lines approximately enclose the wavelength integration range of the W1 filter.

given that the R_p -values have errorbars at least larger than the characteristic depth of the absorption feature. Below we provide evidence that the W1 may be sensitive to the $3\text{-}\mu\text{m}$ feature.

Our first step was to assemble VNIR spectra up to $\sim 3.6 \mu\text{m}$ of a list of nine C-complex control asteroids. All of these asteroids are primitive, including some B-types, such as (2) Pallas or (45) Eugenia, and some of them show a distinct absorption feature. The assembled spectra are plotted along with the best-fit value of R_p in Fig. 6. We collected or digitised data from Hiroi et al. (1996), SMASS-II (Bus & Binzel 2002), the 52-Color Survey (Bell et al. 2005), Rivkin et al. (2003) and de León et al. (2012). Taking into account the errors associated with superimposing spectra obtained at different epochs of observation with different equipment and the uncertainties in the spectra and in the value of the albedo ratio, the latter is not expected to exactly match the value of the spectra at $3.4 \mu\text{m}$. Owing to these deviations, seen in Fig. 6, one cannot confirm nor rule out the presence of the absorption feature based on the value of R_p alone.

Next, we combined the values of R_p with the observed relative reflectances at $2.5 \mu\text{m}$ available from other datasets. Rivkin et al. (2003) use the parameter $1 - R_\lambda/R_{2.5}$ as a rough measure of band depth. Because the band minima are usually near $3.0 \mu\text{m}$ and given that W1 results from an average over 2.8 to $3.8 \mu\text{m}$, the parameter $b \equiv 1 - R_p/R_{2.5}$ is not to be taken as a measure of band depth but as a helpful parameter to quantitatively compare the values of relative reflectances at 2.5 and $3.4 \mu\text{m}$. If a deep absorption band is present, R_p is in general expected to be $\lesssim R_{2.5}$ and hence $b \gtrsim 0$, as is the case of (19) Fortuna. There is one general case for which this interpretation would be wrong: if the NIR slope is negative up to $3.4 \mu\text{m}$, we would have $b \gtrsim 0$ even if no band was present, though blue NIR slopes such as Pallas' have only been measured in a small percentage of cases (e.g. 2 out of 45 in the sample of de León et al. 2012).

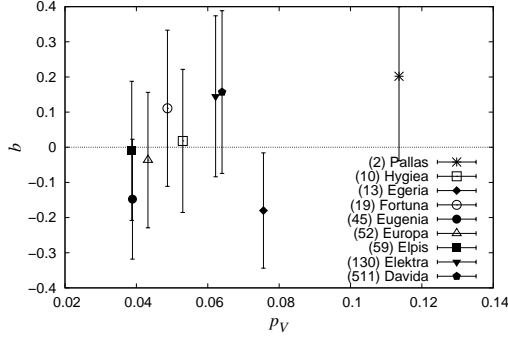


Fig. 7. Plot of $b = 1 - R_p/R_{2.5}$ versus p_V for a set of primitive control objects. The values of b obtained from the combination of our R_p and the $R_{2.5}$ taken from the assembly of spectra published by other authors (cf. figure 6) and the shape of the $3 \mu\text{m}$ absorption band are consistent except for (13) Egeria.

A plot of b vs. p_V is shown in Fig. 7 with an estimated b errorbar of 0.2 to account for the large uncertainties in R_p and the assembly of the spectra. We see that those asteroids with a weak or non-existent absorption band tend to have $b \lesssim 0$, whereas $b \gtrsim 0$ for those with a higher-contrast feature. Only in the case of (13) Egeria the value of b is clearly inconsistent with the absorption band observed. Indeed, the large errorbar in the value of b still prevents irrefutable detection of the band on a case-by-case basis, but from Fig. 7, the correlation between the sign of b and the spectra appears robust, so that systematically obtaining $b \gtrsim 0$ for a given population may be statistically significant.

In Fig. 8 (left panel) we show a b -value histogram of those B type asteroids for which the value of b could be determined. $R_{2.5}$ was taken from the B-type spectra presented in de León et al. (2012), after normalising to unity at $0.55 \mu\text{m}$. In order to test for statistical significance, we resort to the Kolmogorov-Smirnov (KS) test, which enables one to reject the null hypothesis that a given set of unbinned values is compatible with having been drawn from a given distribution function (see e.g. Press et al. 1986). As the null hypothesis we take a gaussian distribution with zero mean. This choice is based on the mean value of b that we would expect considering that interpolating between $R_{0.55} = 1$ and $\bar{R}_p = 1$ gives $\bar{R}_{2.5} = 1.0 \Rightarrow \bar{b} = 0$ (see Fig. 9). The KS test amply rules out the null hypothesis that the B-types b -values are drawn from a gaussian distribution of zero mean regardless of its width (σ).

To demonstrate the robustness of this result even further, we carried out the same procedure for a list of asteroids belonging to the S-complex, including all Bus-DeMeo pure S-types for which we found the value of $R_{2.5}$ was available from the literature and for which R_p could be computed, plus enough randomly selected S subtypes to get the same number of b -values we derived for the B-types (see Table 4). S-type asteroids are “anhydrous” and have positive spectral slopes up to $2.5 \mu\text{m}$ so that in the absence of a $3\text{-}\mu\text{m}$ absorption feature one would expect a negative value of b if the spectral slope maintains its trend up to $3.4 \mu\text{m}$. Taking into account that $\bar{R}_p \approx 1.67$ for this sample of S-types, from the interpolated value $\bar{R}_{2.5} \approx 1.46$ (see Table 3), the expected mean value of b would be $\bar{b} = -0.14$ (see Fig. 9). The distribution of b -values obtained for the S-types, shown in the right panel of Fig. 8, presents a negative mean value. In this case, the KS test does not rule out the null hypothesis that the b -values are drawn from a Gaussian distribution centered at -0.14

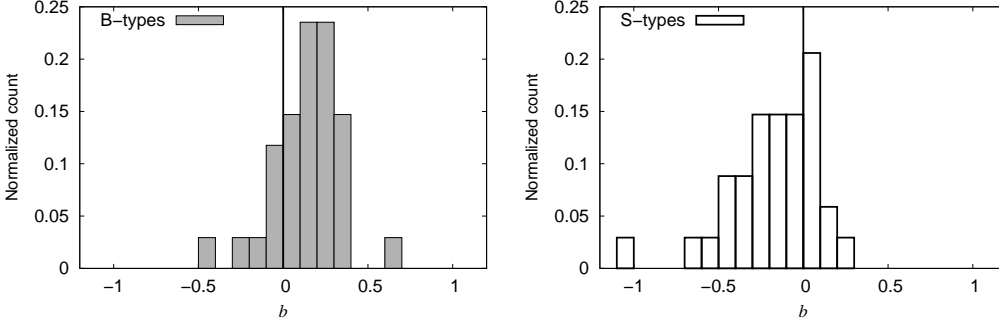


Fig. 8. Normalised histograms showing the distribution of b -values. Left panel: B-types; the fact that $b > 0$ in the majority of cases suggests that a large percentage of these asteroids have absorption features in the $\sim 3\text{-}\mu\text{m}$ region. Right panel: S-types; the opposite conclusion is reached, consistent with the anhydrous nature of S-types.

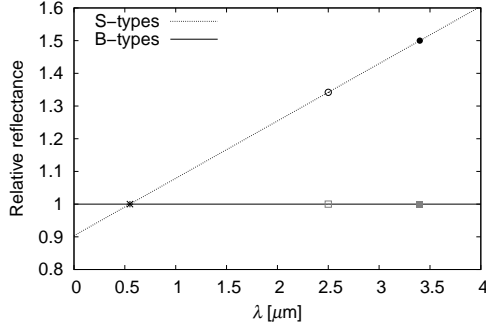


Fig. 9. Schematic diagram illustrating the interpolation of $R_{2.5}$ (empty points) from the average values of R_p (filled points) for the B and S asteroids studied.

with $\sigma = 0.2$ with p -value > 0.9 . This rules out the possibility that a systematic error is causing the b -values of the B-type asteroids to be > 0 .

Table 4. Median and standard deviation of b -values for B-types and S-types

Group	Median	σ	N
B-types	0.2	0.2	34
S-types	-0.2	0.2	34

In the preceding subsection we showed that our values of R_p are systematically $\sim 10\%$ lower than those of Masiero et al. (2011). We carried out the same procedure enlarging our R_p values 10% and the conclusions still hold.

To conclude, we find that the majority of B-types with computed b -values verify $b > 0$ and that very few present a clearly negative value of b , which means that even for those B-type spectra with a positive slope in the $2.5\ \mu\text{m}$ region (approximately half of the objects in de León et al. 2012) there is a reduction in the reflectivity around $3.4\ \mu\text{m}$. As discussed above, for asteroids of the C-complex, the $3\text{-}\mu\text{m}$ absorption feature has been attributed to hydrated minerals or water-ice. The presence of goethite has been also proposed as an alternative explanation for this band (Beck et al.

2011). Nonetheless, while other closely related minerals have been found in both meteorite and asteroid spectra, extraterrestrial goethite has never been identified within the meteorite inventory, so the possibility that putative goethite-containing asteroids never found a dynamical collisional pathway to Earth is less likely than the simpler interpretation: goethite is not present in asteroidal surfaces (Jewitt & Guilbert-Lepoutre 2012). Therefore, from the distribution of b -values, we conclude that most asteroids in this sample (which constitutes $\lesssim 40\%$ of the B-type population with computed R_p) present this absorption and that “water” (be it bound or free) may be common among the B-type asteroids.

4.3. The Pallas collisional family

We use the most up-to-date Pallas family list by (Nesvorný 2012). WISE has observed 46 of the objects in this list. Histograms of beaming parameter and albedo determinations are shown in Fig. 10 (the complete set of parameters is shown in Table 4). Given that the R_p value could only be fitted for seven objects, we do not include histograms for R_p and p_{IR} . In Table 6 we present the mean values of η , p_V and R_p along with their corresponding standard deviations and contributing number of determinations.

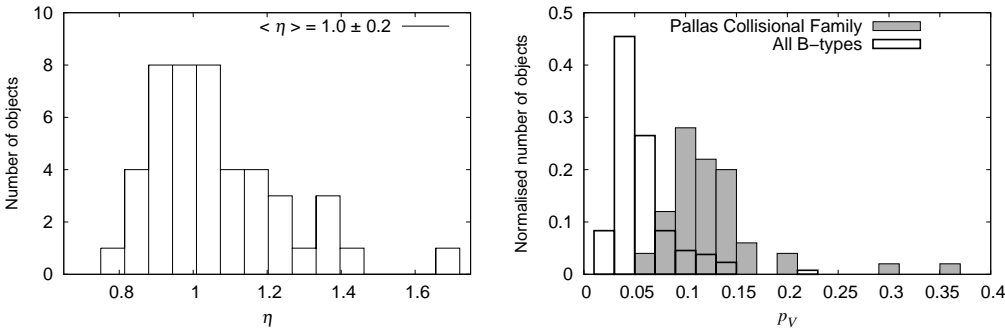


Fig. 10. Beaming parameter (left) and geometric albedo (right) distributions of the values derived for the PCF members observed by WISE. The albedo distributions are normalised, i.e. divided by their respective total number of counts.

Table 6. Mean values and standard deviations of η , R_p and p_V derived for the members of the Pallas collisional family observed by WISE.

Parameter	Mean Value	σ	N
η	1.0	0.2	46
R_p	0.5	0.1	7
p_V	0.14	0.05	50

The average η value of the PCF is consistent with that of the B-type population and that of the Main Belt (Masiero et al. 2011). However, the PCF has a moderately high albedo of $\sim 14\%$, significantly higher than the rest of the B-types and indeed higher than the value expected for primitive asteroids, whereas their average R_p is lower than the average value for the B-types (cf. Table

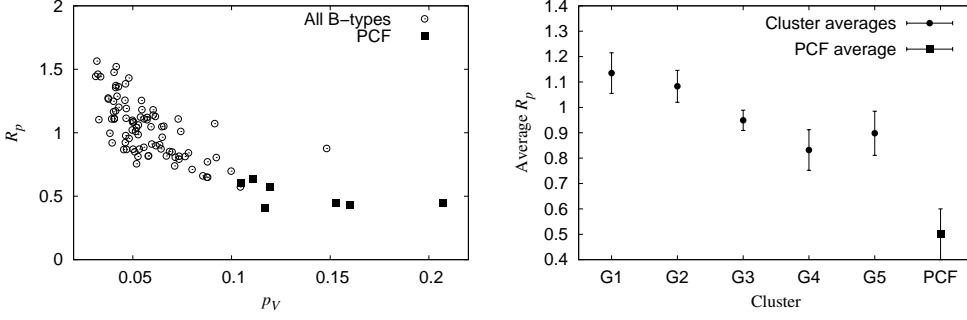


Fig. 11. Left panel: PCF members are on average brighter in the visible and bluer in the $3.4 \mu\text{m}$ region than the B-types sample (cf. Fig. 3). The 20% errorbars are not plotted for clarity. Right panel: the average R_p of the PCF continues the decreasing trend of the de León et al. (2012) clusters (cf. Fig. 5).

2). The seven R_p -values computed are quite homogeneous compared to the distribution observed for the rest of the B-type population. As we saw in Sect. 4.1, our parameter determinations are consistent within the errorbars with those of (Masiero et al. 2011), so we do not perform the same comparison for the PCF members. Masiero et al. show a histogram of $\log p_V$ with peak between $\log p_V = (-1) - (-0.8)$, i.e. $p_V = 0.10-0.16$, with which our results are consistent (they provide no mean value to compare with). On the other hand, though they provide the best-fit parameters in their Table 1, Masiero et al. do not discuss the R_p values of the PCF.

The average p_V and R_p values continue the trend observed for the clusters of de León et al. (2012) in Fig. 4 and Fig. 5: they have higher visible albedos on average than the G5 cluster and are bluer at $3.4 \mu\text{m}$ than the bluest cluster, G4 (note that the average R_p value of cluster G5 is obtained from only three objects, which could explain its deviation from the trend). Members of the Pallas-like group of objects of Clark et al. (2010) were concentrated in clusters G4 and G5 in de León et al. (2012) (see Sect. 1). In this work, the list of Pallas family members observed by WISE includes yet more asteroids. The four additional objects with R_p determinations that were not present in de León et al. (2012) are also located in the lower right region of Fig. 4. This property would be consistent with the characteristics of an extrapolated G6 centroid (see the right panel of Fig. 11). Interestingly, the G6 centroid of de León et al. (2012) contained asteroid (3200) Phaethon alone. Therefore, the connection of the NEA (3200) Phaethon to the Pallas Collisional Family established by de León et al. (2010) based on spectroscopical and dynamical arguments is also supported by the values of relative reflectances at $3.4 \mu\text{m}$.

5. Discussion

In Sect. 4.2 we present statistically significant indications that water may be common within our sample, and in Sect. 4.3 we point out how the PCF have higher geometric visible albedos and more homogeneously distributed R_p -values than the rest of B-types. The purpose of this section is to put these results in the context of other studies in the literature.

In the context of the geophysical models of the Themis and Pallas parent bodies by Castillo-Rogez & Schmidt (2010) and Schmidt & Castillo-Rogez (2012), the detections of water ice and organics on the surface of (24) Themis (Rivkin & Emery 2010; Campins et al. 2010b) and

(65) Cybele (Licandro et al. 2011) have been invoked as provocative indications that water has played an important role in the accretion and evolution of these asteroids' parent bodies in the mid-outer asteroid belt. Finding indications that a $3\text{-}\mu\text{m}$ is frequently present in B-types spectra adds further support to this conceptual framework, in which the gradual differences in the observed NIR spectral slopes of B-types might also be explained as resulting from different subsequent evolution and processing of their parent bodies.

Schmidt & Castillo-Rogez (2012) discuss that (1) Ceres, being the largest body of the asteroid belt and plausibly a water-rich asteroid, mostly preserved its integrity, whereas the Themis parent body was catastrophically disrupted. Pallas would be an intermediate case, still intact but showing evidence for heating, internal evolution, impact and loss of water. In accordance with this scenario, the Themis family members included in the de León et al. (2012) sample were distributed more or less homogeneously among the representative centroids of the complete sample, spanning from neutral to red slopes and matching several meteorite analogues, whereas the PCF members were concentrated in the bluest centroids. As our results show, these trends are also verified longward of $2.5\ \mu\text{m}$: the Themis family members show more heterogeneous R_p values whereas the Pallas family members have distinctly higher albedos and lower, more homogeneous values of R_p than the rest of B-types. This homogeneity is consistent with the collisional family being the result of a non-disruptive cratering event on Pallas, which has a significantly higher albedo than the rest of large B-types.

The geophysical models by Schmidt & Castillo-Rogez (2012) favour a water-rich past for Pallas. Its near spherical shape may be explained as a consequence of early melting of a substantial initial icy component that is subsequently removed by a combination of thermal and impacts processes. The water-loss processes that took place on the surface of Pallas may have taken place on other active bodies such as main belt comets or indeed (3200) Phaethon, linked to the Pallas collisional family by de León et al. (2010), and this activity has already been proposed to explain the characteristic NIR blue spectral slope (Schmidt & Castillo-Rogez 2012, and references therein). According to this model, water-rich materials are also expected to be important components within some members of Pallas' family. The fact that the PCF members in this study are found to match the properties of the least hydrated clusters of de León et al. (2012) would be inconsistent with this view, but caution must be exercised when associating NIR slopes of meteorite analogues to hydration. For instance, while having suffered intense thermal metamorphism, CK4 chondrites (the best matches for Pallas) still show an absorption feature at $2.9\ \mu\text{m}$, albeit less prominent than e.g. CM chondrites.

From the dynamical standpoint, the simulations of Walsh et al. (2011) also provide a congruous context for our results. Their model suggests that C-complex asteroids were formed in the giant-planet-forming region and that, for every C-type planetesimal from beyond 8 AU that would later be located in the outer Main Belt, > 10 would have ended up in the region where terrestrial planets formed. Assuming that the composition of these objects is 10% water by mass, this may account for the minimal mass required to bring the current amount of water to our planet by a factor of 6–22.

On the other hand, the question of the moderately high values of p_V obtained for the PCF remains unanswered. Finding members of the Pallas and Themis collisional families distributed differently among the de León et al. (2012) clusters and in Fig. 11 (as discussed above) also leads

us to ponder the possibility that a sequential or progressive physical process could explain the differences in the value distributions of p_V and R_p . Unfortunately, there are many possible mechanisms underlying the observed NIR spectral variability of primitive asteroids (e.g. regolith particle sizes, space weathering as a function of asteroid family age and composition, thermal processing) and these are difficult to disentangle (Ziffer et al. 2011).

6. Conclusions

We have derived values of D , η , and R_p of 111 B-type asteroids by means of thermal modelling of WISE data and updated H values (most of which have increased since the work of Masiero et al. 2011, as shown in Fig. 1). Additionally, from H and D we have computed the corresponding values of p_V (Table 2). Our results are in agreement within the errorbars of the model with those previously published by Masiero et al. (2011). However, we obtain a systematic trend of approximately -10% discrepancies in the determinations of R_p that we cannot explain but is most probably attributable to small differences in the tabulated solar flux data necessary to estimate the reflected light component at $3.4 \mu\text{m}$. This work led to the following conclusions:

1. We derived the distribution of η , p_V and R_p for the B-type asteroids (see Fig. 2) and obtained the following mean values: $\bar{\eta} = 1.0 \pm 0.1$, $\bar{p}_V = 0.07 \pm 0.03$, and $\bar{R}_p = 1.0 \pm 0.3$.
2. There are no high- p_V , high- R_p B-type asteroids ($p_V > 0.10$, $R_p > 1.0$; see Fig. 3). The average R_p -values of the centroids of de León et al. (2012) clearly decrease from G1 to G5, which implies a relationship between the IR slope of the asteroid spectra up to $2.5 \mu\text{m}$ (Figs. 4 and 5).
3. We computed b -values for a set of B-type asteroids and S-complex asteroids, which present $\bar{b} > 0$ and $\bar{b} < 0$, respectively (Fig. 8). While the latter result is consistent with objects of the S-complex being anhydrous, the former indicates that the majority of B-type asteroids b -values in this study are consistent with the presence of a $3\text{-}\mu\text{m}$ absorption feature usually attributed to hydrated minerals or water-ice; therefore, water must have played a key role in the evolution of a large fraction of the B-types, supporting recent works discussed in Sect. 5.
4. We have also studied the Pallas collisional family. On the one hand, the average albedo ($\bar{p}_V = 0.14 \pm 0.05$) of this family is significantly higher than the average albedo of B-types ($\bar{p}_V = 0.07 \pm 0.03$) and moderately high compared to what is traditionally considered to be the albedo of primitive asteroids (< 0.1). On the other hand, the albedo ratio values of the PCF members are very low and homogeneous ($\bar{R}_p = 0.5 \pm 0.1$). These results clearly show the fundamental differences between the Pallas Collisional Family and the rest of B-types.

In addition, the connection of the NEA (3200) Phaethon to the Pallas Collisional Family established by de León et al. (2010) based on spectroscopical and dynamical arguments is also supported by the values of relative reflectances at $3.4 \mu\text{m}$.

5. Our results support the scenarios by the geophysical models by Castillo-Rogez & Schmidt (2010) and Schmidt & Castillo-Rogez (2012) and the simulations of Walsh et al. (2011), which suggest that water played an important role in the origin of primitive asteroid parent bodies of the mid-outer belt.

Acknowledgements. We thank the referee for a careful and constructive revision. VAL acknowledges support from the project AYA2011-29489-C03-02 (MEC). JL acknowledges support from the projects AYA2011-29489-C03-02 and AYA2012-39115-C03-03 (MINECO). JdL thanks financial support via a "Juan de la Cierva" contract from the Spanish

“Secretaría de Estado de Investigación, Desarrollo e Innovación”. MDB thanks the Space Situation Awareness program of the European Space Agency (ESA-SSA) for financial support. NPA was financed by the Spanish Ministry of Economy and Competitiveness throughout the Juan de la Cierva program.

This publication makes use of data products from NEOWISE, which is a project of the Jet Propulsion Laboratory/California Institute of Technology, funded by the Planetary Science Division of the National Aeronautics and Space Administration. This research has also made use of the NASA/IPAC Infrared Science Archive, which is operated by the Jet Propulsion Laboratory, California Institute of Technology, under contract with the National Aeronautics and Space Administration.

References

- Barucci, M. A., Cheng, A. F., Michel, P., et al. 2012, *Experimental Astronomy*, 33, 645
- Beck, P., Quirico, E., Sevestre, D., et al. 2011, *A&A*, 526, A85
- Bell, J. F., Owensby, P. D., Hawke, B. R., et al. 2005, *NASA Planetary Data System*, 28
- Bowell, E., Hapke, B., Domingue, D., et al. 1989, in *Asteroids II*, ed. R. P. Binzel, T. Gehrels, & M. S. Matthews, 524–556
- Bus, S. J. & Binzel, R. P. 2002, *Icarus*, 158, 146
- Campins, H., Hargrove, K., Pinilla-Alonso, N., et al. 2010a, *Nature*, 464, 1320
- Campins, H., Morbidelli, A., Tsiganis, K., et al. 2010b, *ApJ*, 721, L53
- Castillo-Rogez, J. C. & Schmidt, B. E. 2010, *Geophys. Res. Lett.*, 37, 10202
- Clark, B. E., Ziffer, J., Nesvornyy, D., et al. 2010, *Journal of Geophysical Research (Planets)*, 115, 6005
- Cutri et al., R. M. 2012, *VizieR Online Data Catalog*, 2311, 0
- de León, J., Campins, H., Tsiganis, K., Morbidelli, A., & Licandro, J. 2010, *A&A*, 513, A26
- de León, J., Mothé-Diniz, T., Licandro, J., Pinilla-Alonso, N., & Campins, H. 2011, *A&A*, 530, L12
- de León, J., Pinilla-Alonso, N., Campins, H., Licandro, J., & Marzo, G. A. 2012, *Icarus*, 218, 196
- Delbó, M., Dell’Oro, A., Harris, A. W., Mottola, S., & Mueller, M. 2007, *Icarus*, 190, 236
- Delbó, M. & Harris, A. W. 2002, *Meteoritics and Planetary Science*, 37, 1929
- DeMeo, F. E., Binzel, R. P., Slivan, S. M., & Bus, S. J. 2009, *Icarus*, 202, 160
- Gaffey, M. J., Bell, J. F., & Cruikshank, D. P. 1989, in *Asteroids II*, ed. R. P. Binzel, T. Gehrels, & M. S. Matthews, 98–127
- Gaffey, M. J., Cloutis, E. A., Kelley, M. S., & Reed, K. L. 2002, *Asteroids III*, 183
- Gil-Hutton, R. 2006, *Icarus*, 183, 93
- Grav, T., Mainzer, A. K., Bauer, J., et al. 2012, *ApJ*, 744, 197
- Harris, A. W. 1998, *Icarus*, 131, 291
- Harris, A. W. 2006, in *IAU Symposium*, Vol. 229, *Asteroids, Comets, Meteors*, ed. L. Daniela, M. Sylvio Ferraz, & F. J. Angel, 449–463
- Hiroi, T., Zolensky, M. E., Pieters, C. M., & Lipschutz, M. E. 1996, *Meteoritics and Planetary Science*, 31, 321
- Jewitt, D. & Guilbert-Lepoutre, A. 2012, *AJ*, 143, 21
- Lauretta, D. S., Drake, M. J., Benz, R. P., et al. 2010, *Meteoritics and Planetary Science Supplement*, 73, 5153
- Licandro, J., Campins, H., Kelley, M., et al. 2011, *A&A*, 525, A34
- Licandro, J., Hargrove, K., Kelley, M., et al. 2012, *A&A*, 537, A73
- Mainzer, A., Bauer, J., Grav, T., et al. 2011a, *ApJ*, 731, 53
- Mainzer, A., Grav, T., Masiero, J., et al. 2011b, *ApJ*, 736, 100
- Mainzer, A., Grav, T., Masiero, J., et al. 2011c, *ApJ*, 741, 90
- Marzo, G. A., Roush, T. L., & Hogan, R. C. 2009, *Journal of Geophysical Research (Planets)*, 114, 8001
- Masiero, J. R., Mainzer, A. K., Grav, T., et al. 2011, *ApJ*, 741, 68
- Maurette, M. 2006, *Micrometeorites and the Mysteries of Our Origins* (Berlin: Springer-Verlag)
- Neckel, H. & Labs, D. 1984, *Sol. Phys.*, 90, 205
- Nesvornyy, D. 2012, *NASA Planetary Data System*, 189
- Pieters, C. M. & Hiroi, T. 2004, in *Lunar and Planetary Institute Science Conference Abstracts*, Vol. 35, *Lunar and Planetary Institute Science Conference Abstracts*, ed. S. Mackwell & E. Stansbery, 1720
- Press, W. H., Flannery, B. P., & Teukolsky, S. A. 1986, *Numerical recipes. The art of scientific computing*
- Rivkin, A. S., Davies, J. K., Johnson, J. R., et al. 2003, *Meteoritics and Planetary Science*, 38, 1383
- Rivkin, A. S. & Emery, J. P. 2010, *Nature*, 464, 1322

- Rivkin, A. S., Howell, E. S., Lebofsky, L. A., Clark, B. E., & Britt, D. T. 2000, *Icarus*, 145, 351
- Schmidt, B. E. & Castillo-Rogez, J. C. 2012, *Icarus*, 218, 478
- Tholen, D. J. 1984, PhD thesis, Arizona Univ., Tucson.
- Tholen, D. J. 1989, in *Asteroids II*, ed. R. P. Binzel, T. Gehrels, & M. S. Matthews, 1139–1150
- Vilas, F. & Gaffey, M. J. 1989, *Science*, 246, 790
- Vilas, F., Jarvis, K. S., & Gaffey, M. J. 1994, *Icarus*, 109, 274
- Walsh, K. J., Morbidelli, A., Raymond, S. N., O'Brien, D. P., & Mandell, A. M. 2011, *Nature*, 475, 206
- Wright, E. L., Eisenhardt, P. R. M., Mainzer, A. K., et al. 2010, *AJ*, 140, 1868
- Ziffer, J., Campins, H., Licandro, J., et al. 2011, *Icarus*, 213, 538

Table 1. Best-fitting values of physical parameters determined for the B-types with WISE observations. Negative values of η and or R_p indicate that the parameter was not free but fixed to the corresponding positive value. Errorbars shown are minimum estimates and correspond to 10% relative error for D and 20% for η , p_V and R_p .

Designation	H	G	D [km]	p_V	η	R_p	W1	W2	W3	W4	$R_{2.5}$
00002	4.13	0.11	669 ± 67	0.09 ± 0.02	-1.0 ± 0.2	0.8 ± 0.2	3	3	0	0	0.8
00024	7.08	0.19	187 ± 19	0.07 ± 0.01	-1.0 ± 0.2	1.0 ± 0.2	5	5	0	0	1.1
00045	7.46	0.07	240 ± 24	0.03 ± 0.01	-1.0 ± 0.2	1.6 ± 0.3	9	10	0	0	1.3
00047	7.84	0.16	118 ± 12	0.09 ± 0.02	-1.0 ± 0.2	0.8 ± 0.2	9	9	0	0	-
00052	6.31	0.18	396 ± 40	0.03 ± 0.01	-1.0 ± 0.2	1.4 ± 0.3	4	4	0	0	1.3
00059	7.93	0.15	169 ± 17	0.04 ± 0.01	-1.0 ± 0.2	1.4 ± 0.3	11	11	0	0	1.3
00085	7.61	0.15	148 ± 15	0.07 ± 0.01	-1.0 ± 0.2	1.1 ± 0.2	6	6	0	0	1.1
00141	8.40	0.15	129 ± 13	0.05 ± 0.01	-1.0 ± 0.2	1.0 ± 0.2	9	9	0	0	-
00142	10.27	0.15	58 ± 6	0.04 ± 0.01	1.0 ± 0.2	1.1 ± 0.2	8	8	0	8	1.1
00225	8.72	0.15	107 ± 11	0.05 ± 0.01	1.1 ± 0.2	1.1 ± 0.2	14	15	15	14	-
00229	9.13	0.15	110 ± 11	0.03 ± 0.01	0.8 ± 0.2	1.5 ± 0.3	10	10	0	10	-
00241	7.58	0.15	189 ± 19	0.05 ± 0.01	-1.0 ± 0.2	1.3 ± 0.3	7	7	0	0	-
00241	7.58	0.15	198 ± 20	0.04 ± 0.01	-1.0 ± 0.2	1.3 ± 0.3	7	7	0	0	-
00268	8.28	0.15	142 ± 14	0.04 ± 0.01	-1.0 ± 0.2	1.4 ± 0.3	9	9	0	0	-
00282	10.91	0.15	41 ± 4	0.05 ± 0.01	1.0 ± 0.2	-1.5 ± 0.3	10	10	0	10	-
00314	9.80	0.15	64 ± 6	0.05 ± 0.01	1.0 ± 0.2	1.0 ± 0.2	14	14	0	14	-
00335	8.96	0.15	88 ± 9	0.06 ± 0.01	1.1 ± 0.2	0.9 ± 0.2	4	4	0	4	1.1
00357	8.72	0.15	105 ± 10	0.05 ± 0.01	1.0 ± 0.2	0.8 ± 0.2	8	8	0	8	1.1
00372	7.50	0.15	180 ± 18	0.05 ± 0.01	-1.0 ± 0.2	1.3 ± 0.3	12	12	0	0	-
00379	8.87	0.15	88 ± 9	0.06 ± 0.01	1.0 ± 0.2	1.0 ± 0.2	6	6	0	6	1.2
00383	9.91	0.15	44 ± 4	0.10 ± 0.02	1.3 ± 0.2	0.7 ± 0.1	12	13	13	13	0.9
00400	10.50	0.15	39 ± 4	0.07 ± 0.01	1.2 ± 0.2	0.8 ± 0.2	11	11	11	10	-
00404	9.01	0.15	98 ± 10	0.05 ± 0.01	1.0 ± 0.2	0.9 ± 0.2	8	8	0	8	-
00426	8.42	0.15	117 ± 12	0.06 ± 0.01	0.9 ± 0.2	1.1 ± 0.2	9	9	0	6	0.8
00431	8.72	0.15	103 ± 10	0.05 ± 0.01	0.9 ± 0.2	1.1 ± 0.2	13	12	0	12	1.2
00461	10.48	0.15	46 ± 5	0.05 ± 0.01	1.0 ± 0.2	1.1 ± 0.2	26	27	27	27	-
00464	9.52	0.15	84 ± 8	0.04 ± 0.01	1.0 ± 0.2	1.1 ± 0.2	4	4	0	4	-
00464	9.52	0.15	82 ± 8	0.04 ± 0.01	0.9 ± 0.2	1.2 ± 0.2	26	26	0	26	-
00468	9.83	0.15	66 ± 7	0.05 ± 0.01	1.0 ± 0.2	1.2 ± 0.2	13	13	0	13	-
00526	10.17	0.15	48 ± 5	0.06 ± 0.01	1.1 ± 0.2	0.9 ± 0.2	13	12	17	17	-
00531	12.00	0.15	16 ± 2	0.10 ± 0.02	0.9 ± 0.2	-1.5 ± 0.3	0	8	12	12	-
00541	10.10	0.15	57 ± 6	0.05 ± 0.01	1.0 ± 0.2	1.0 ± 0.2	13	11	0	13	-
00555	10.70	0.15	33 ± 3	0.09 ± 0.02	1.0 ± 0.2	0.7 ± 0.1	12	12	12	12	-
00560	10.90	0.15	36 ± 4	0.06 ± 0.01	1.0 ± 0.2	0.8 ± 0.2	14	14	9	14	-
00567	9.16	0.15	91 ± 9	0.05 ± 0.01	1.0 ± 0.2	1.4 ± 0.3	8	8	0	7	-
00567	9.16	0.15	82 ± 8	0.06 ± 0.01	1.0 ± 0.2	1.1 ± 0.2	8	8	0	8	-
00635	9.01	0.15	97 ± 10	0.05 ± 0.01	0.9 ± 0.2	0.9 ± 0.2	11	11	0	8	-
00702	7.25	0.15	202 ± 20	0.05 ± 0.01	-1.0 ± 0.2	1.2 ± 0.2	10	10	0	0	-
00704	5.94	-0.02	361 ± 36	0.06 ± 0.01	-1.0 ± 0.2	1.1 ± 0.2	6	7	0	0	-
00704	5.94	-0.02	351 ± 35	0.06 ± 0.01	-1.0 ± 0.2	1.1 ± 0.2	8	8	0	0	-

Table 1. continued.

Designation	H	G	D [km]	p_V	η	R_p	W1	W2	W3	W4	$R_{2.5}$
00762	8.28	0.15	144 ± 14	0.04 ± 0.01	-1.0 ± 0.2	1.4 ± 0.3	10	10	0	0	-
00767	10.10	0.15	47 ± 5	0.07 ± 0.01	1.1 ± 0.2	0.8 ± 0.2	9	12	12	12	1.0
00893	9.47	0.15	76 ± 8	0.05 ± 0.01	0.9 ± 0.2	1.1 ± 0.2	8	9	0	9	-
00895	8.20	0.15	123 ± 12	0.06 ± 0.01	1.1 ± 0.2	0.9 ± 0.2	7	7	0	7	-
00954	9.94	0.15	52 ± 5	0.07 ± 0.01	1.1 ± 0.2	0.9 ± 0.2	12	12	0	12	-
00981	10.57	0.15	34 ± 3	0.09 ± 0.02	1.1 ± 0.2	0.6 ± 0.1	7	8	8	8	-
00988	11.60	0.15	22 ± 2	0.08 ± 0.02	0.9 ± 0.2	-1.5 ± 0.3	0	0	10	10	-
00988	11.60	0.15	22 ± 2	0.09 ± 0.02	0.9 ± 0.2	-1.5 ± 0.3	0	0	10	10	-
01003	10.70	0.15	36 ± 4	0.07 ± 0.01	1.3 ± 0.2	0.8 ± 0.2	8	8	8	8	1.0
01003	10.70	0.15	34 ± 3	0.08 ± 0.02	1.4 ± 0.2	0.8 ± 0.2	12	8	13	13	1.0
01021	8.98	0.15	105 ± 11	0.04 ± 0.01	1.0 ± 0.2	1.1 ± 0.2	12	12	0	12	1.0
01035	10.20	0.15	60 ± 6	0.04 ± 0.01	1.0 ± 0.2	1.3 ± 0.2	12	14	14	14	1.4
01076	12.30	0.15	24 ± 2	0.04 ± 0.01	1.0 ± 0.2	1.0 ± 0.2	5	7	8	8	1.0
01076	12.30	0.15	23 ± 2	0.04 ± 0.01	0.9 ± 0.2	0.9 ± 0.2	13	13	13	13	1.0
01109	10.06	0.15	64 ± 6	0.04 ± 0.01	0.9 ± 0.2	1.5 ± 0.3	11	11	0	11	-
01109	10.06	0.15	63 ± 6	0.04 ± 0.01	0.9 ± 0.2	1.5 ± 0.3	7	7	0	7	-
01154	10.51	0.15	59 ± 6	0.03 ± 0.01	1.0 ± 0.2	1.4 ± 0.3	11	12	9	12	-
01213	11.10	0.15	31 ± 3	0.06 ± 0.01	1.1 ± 0.2	1.0 ± 0.2	12	13	15	15	-
01229	11.30	0.15	30 ± 3	0.06 ± 0.01	1.1 ± 0.2	1.2 ± 0.2	7	0	13	13	-
01331	10.14	0.15	39 ± 4	0.10 ± 0.02	1.1 ± 0.2	0.6 ± 0.1	13	14	14	14	-
01340	11.10	0.15	32 ± 3	0.06 ± 0.01	1.2 ± 0.2	0.9 ± 0.2	7	9	9	9	-
01362	11.18	0.15	30 ± 3	0.07 ± 0.01	1.1 ± 0.2	-1.5 ± 0.3	0	0	12	12	-
01444	11.30	0.15	28 ± 3	0.07 ± 0.01	1.0 ± 0.2	-1.5 ± 0.3	0	0	15	15	-
01474	12.66	0.15	15 ± 2	0.06 ± 0.01	0.8 ± 0.2	-1.5 ± 0.3	0	0	8	8	-
01474	12.66	0.15	15 ± 2	0.07 ± 0.01	0.8 ± 0.2	-1.5 ± 0.3	0	0	6	6	-
01484	10.80	0.15	41 ± 4	0.05 ± 0.01	0.9 ± 0.2	1.0 ± 0.2	11	11	0	11	1.5
01493	11.99	0.15	23 ± 2	0.05 ± 0.01	0.9 ± 0.2	-1.5 ± 0.3	17	17	0	17	-
01508	12.03	0.15	16 ± 2	0.11 ± 0.02	1.0 ± 0.2	-1.5 ± 0.3	0	0	5	5	-
01539	11.10	0.15	26 ± 3	0.09 ± 0.02	1.0 ± 0.2	1.1 ± 0.2	8	0	12	12	1.1
01576	11.04	0.15	30 ± 3	0.08 ± 0.02	1.2 ± 0.2	0.8 ± 0.2	8	8	8	8	-
01579	10.68	0.15	50 ± 5	0.04 ± 0.01	0.9 ± 0.2	1.2 ± 0.3	9	10	12	12	-
01615	11.38	0.15	31 ± 3	0.05 ± 0.01	1.1 ± 0.2	0.9 ± 0.2	11	13	12	12	-
01655	11.04	0.15	40 ± 4	0.04 ± 0.01	1.0 ± 0.2	1.2 ± 0.2	11	12	12	12	1.4
01655	11.04	0.15	38 ± 4	0.05 ± 0.01	1.0 ± 0.2	1.1 ± 0.2	11	11	11	11	1.4
01693	10.97	0.15	39 ± 4	0.05 ± 0.01	0.9 ± 0.2	1.0 ± 0.2	11	11	0	11	-
01705	13.20	0.15	11 ± 1	0.07 ± 0.01	1.0 ± 0.2	-1.5 ± 0.3	0	6	9	9	-
01705	13.20	0.15	13 ± 1	0.06 ± 0.01	1.1 ± 0.2	-1.5 ± 0.3	0	27	26	27	-
01724	11.30	0.15	40 ± 4	0.03 ± 0.01	1.0 ± 0.2	1.1 ± 0.2	6	10	10	10	-
01768	12.70	0.15	21 ± 2	0.03 ± 0.01	1.0 ± 0.2	-1.5 ± 0.3	0	8	8	8	-
01768	12.70	0.15	20 ± 2	0.04 ± 0.01	1.0 ± 0.2	-1.5 ± 0.3	0	12	12	12	-
01796	9.84	0.15	71 ± 7	0.04 ± 0.01	0.9 ± 0.2	1.2 ± 0.2	17	16	0	16	-
01901	11.40	0.15	27 ± 3	0.07 ± 0.01	1.0 ± 0.2	1.1 ± 0.2	8	10	11	11	-
02096	13.50	0.15	12 ± 1	0.05 ± 0.01	1.3 ± 0.2	-1.5 ± 0.3	0	0	5	5	-
02332	10.60	0.15	36 ± 4	0.08 ± 0.02	1.1 ± 0.2	0.9 ± 0.1	10	11	11	11	1.3

Table 1. continued.

Designation	H	G	D [km]	p_V	η	R_p	W1	W2	W3	W4	$R_{2.5}$
02332	10.60	0.15	34 ± 3	0.09 ± 0.02	1.1 ± 0.2	0.9 ± 0.1	10	13	13	13	1.3
02446	12.90	0.15	13 ± 1	0.07 ± 0.01	1.2 ± 0.2	0.8 ± 0.2	6	10	10	10	1.2
02446	12.90	0.15	15 ± 2	0.05 ± 0.01	1.2 ± 0.2	0.9 ± 0.2	12	13	13	13	1.2
02464	11.70	0.15	23 ± 2	0.07 ± 0.01	1.1 ± 0.2	-1.5 ± 0.3	0	7	14	14	-
02519	11.50	0.15	22 ± 2	0.09 ± 0.02	1.1 ± 0.2	-1.5 ± 0.3	0	0	13	13	-
02524	11.10	0.15	35 ± 4	0.05 ± 0.01	1.0 ± 0.2	1.0 ± 0.2	10	10	10	10	-
02525	10.90	0.15	33 ± 3	0.07 ± 0.01	1.1 ± 0.2	0.8 ± 0.2	11	12	12	11	-
02629	14.90	0.15	5 ± 1	0.07 ± 0.01	1.2 ± 0.2	0.7 ± 0.1	15	19	19	19	-
02659	11.60	0.15	29 ± 3	0.05 ± 0.01	1.0 ± 0.2	1.3 ± 0.3	8	9	11	11	-
02708	12.00	0.15	22 ± 2	0.06 ± 0.01	1.2 ± 0.2	1.0 ± 0.2	7	13	14	14	1.4
02772	13.60	0.15	10 ± 1	0.07 ± 0.01	0.9 ± 0.2	-1.5 ± 0.3	0	12	13	12	-
02809	13.60	0.15	12 ± 1	0.04 ± 0.01	1.0 ± 0.2	-1.5 ± 0.3	0	12	13	13	-
02973	12.90	0.15	15 ± 1	0.06 ± 0.01	0.9 ± 0.2	-1.5 ± 0.3	0	11	11	11	-
02973	12.90	0.15	12 ± 1	0.08 ± 0.02	0.9 ± 0.2	-1.5 ± 0.3	0	9	11	11	-
03000	13.60	0.15	11 ± 1	0.05 ± 0.01	1.1 ± 0.2	-1.5 ± 0.3	0	0	6	6	-
03000	13.60	0.15	11 ± 1	0.06 ± 0.01	1.0 ± 0.2	-1.5 ± 0.3	0	0	15	15	-
03036	10.30	0.15	47 ± 5	0.06 ± 0.01	1.0 ± 0.2	1.0 ± 0.2	9	10	10	10	1.3
03036	10.30	0.15	51 ± 5	0.05 ± 0.01	1.0 ± 0.2	1.0 ± 0.2	8	8	8	8	1.3
03074	13.60	0.15	10 ± 1	0.06 ± 0.01	1.2 ± 0.2	-1.5 ± 0.3	0	5	9	9	-
03139	10.70	0.15	41 ± 4	0.06 ± 0.01	1.1 ± 0.2	0.9 ± 0.2	10	12	11	10	-
03162	11.30	0.15	31 ± 3	0.05 ± 0.01	1.1 ± 0.2	-1.5 ± 0.2	13	8	16	16	1.3
03162	11.30	0.15	33 ± 3	0.05 ± 0.01	1.1 ± 0.2	0.9 ± 0.2	10	10	10	11	1.3
03204	12.20	0.15	21 ± 2	0.05 ± 0.01	1.2 ± 0.2	-1.5 ± 0.3	0	0	7	7	-
03204	12.20	0.15	20 ± 2	0.06 ± 0.01	1.3 ± 0.2	-1.5 ± 0.3	0	0	7	7	-
03566	12.90	0.15	14 ± 1	0.07 ± 0.01	0.9 ± 0.2	-1.5 ± 0.3	0	5	8	8	-
03579	13.60	0.15	7 ± 1	0.12 ± 0.02	0.9 ± 0.2	0.4 ± 0.1	10	14	13	13	1.0
03579	13.60	0.15	7 ± 1	0.13 ± 0.03	1.0 ± 0.2	-1.5 ± 0.3	0	0	9	9	1.0
03581	12.10	0.15	14 ± 1	0.13 ± 0.03	0.9 ± 0.2	-1.5 ± 0.3	0	0	13	13	-
03627	13.50	0.15	11 ± 1	0.06 ± 0.01	1.0 ± 0.2	-1.5 ± 0.3	0	10	10	10	-
03647	11.50	0.15	28 ± 3	0.06 ± 0.01	1.0 ± 0.2	0.8 ± 0.2	11	12	12	12	-
04100	11.50	0.15	17 ± 2	0.15 ± 0.03	1.0 ± 0.2	0.9 ± 0.2	5	0	11	11	1.1
04396	13.60	0.15	5 ± 1	0.24 ± 0.05	1.1 ± 0.2	-1.5 ± 0.3	0	0	8	8	-
04484	12.30	0.15	16 ± 2	0.08 ± 0.02	1.1 ± 0.2	-1.5 ± 0.3	0	6	9	9	-
04837	11.60	0.15	28 ± 3	0.05 ± 0.01	0.9 ± 0.2	-1.5 ± 0.3	0	0	10	10	-
04955	11.70	0.15	22 ± 2	0.08 ± 0.02	1.2 ± 0.2	-1.5 ± 0.3	0	0	12	12	-
04997	12.70	0.15	10 ± 1	0.16 ± 0.03	1.1 ± 0.2	-1.5 ± 0.3	0	0	10	10	-
05057	12.30	0.15	18 ± 2	0.06 ± 0.01	1.0 ± 0.2	-1.5 ± 0.3	0	0	8	8	-
05133	11.90	0.15	24 ± 2	0.05 ± 0.01	1.1 ± 0.2	-1.5 ± 0.3	0	8	12	12	-
05222	11.30	0.15	19 ± 2	0.15 ± 0.03	1.0 ± 0.2	0.4 ± 0.1	12	13	13	13	-
05234	11.90	0.15	15 ± 1	0.15 ± 0.03	1.0 ± 0.2	-1.5 ± 0.3	0	0	6	6	-
05234	11.90	0.15	14 ± 2	0.13 ± 0.03	0.9 ± 0.2	-1.5 ± 0.3	0	0	10	10	-
05330	12.10	0.15	15 ± 2	0.11 ± 0.02	0.9 ± 0.2	0.6 ± 0.1	9	16	16	15	-
05870	13.20	0.15	9 ± 1	0.11 ± 0.02	1.0 ± 0.2	-1.5 ± 0.3	0	0	5	4	-
06297	12.30	0.15	18 ± 2	0.07 ± 0.01	1.1 ± 0.2	-1.5 ± 0.3	0	0	8	8	-

Table 1. continued.

Designation	H	G	D [km]	p_V	η	R_p	W1	W2	W3	W4	$R_{2.5}$
08518	12.80	0.15	14 ± 1	0.07 ± 0.01	1.1 ± 0.2	-1.5 ± 0.3	0	0	5	5	-
08519	13.60	0.15	7 ± 1	0.12 ± 0.02	1.2 ± 0.2	-1.5 ± 0.3	0	0	11	11	-
08906	12.80	0.15	14 ± 1	0.07 ± 0.01	0.9 ± 0.2	-1.5 ± 0.3	0	0	6	6	-
09219	11.90	0.15	20 ± 2	0.07 ± 0.01	1.3 ± 0.2	-1.5 ± 0.3	0	0	8	8	-

Table 3. Best-fitting values of physical parameters determined for the S-types with sufficient W1 WISE observations and published $2.5 \mu\text{m}$ reflectances. Negative values of η and or R_p indicate that the parameter was not free but fixed to the corresponding positive value. Errorbars shown are minimum estimates and correspond to 10% relative error for D and 20% for η , p_V and R_p .

Designation	H	G	D [km]	p_V	η	R_p	W1	W2	W3	W4	$R_{2.5}$
00009	6.280	0.170	231 ± 23	0.10 ± 0.02	-1.0 ± 0.2	2.1 ± 0.4	8	8	0	0	1.5
00009	6.280	0.170	188 ± 19	0.15 ± 0.03	-1.0 ± 0.2	1.9 ± 0.4	13	13	0	0	1.5
00011	6.550	0.150	171 ± 17	0.14 ± 0.03	-1.0 ± 0.2	1.6 ± 0.3	8	8	0	0	1.4
00017	7.760	0.150	93 ± 9	0.16 ± 0.03	0.9 ± 0.2	1.8 ± 0.4	10	10	0	10	1.5
00026	7.400	0.150	86 ± 9	0.26 ± 0.05	1.1 ± 0.2	1.3 ± 0.3	11	12	0	12	1.4
00029	5.850	0.200	194 ± 19	0.21 ± 0.04	1.0 ± 0.2	1.4 ± 0.3	10	10	0	0	1.3
00030	7.570	0.150	88 ± 9	0.21 ± 0.04	-1.0 ± 0.2	1.8 ± 0.4	11	11	0	0	1.5
00032	7.560	0.150	78 ± 8	0.27 ± 0.05	-1.0 ± 0.2	1.4 ± 0.3	7	7	0	0	1.4
00043	7.930	0.110	76 ± 8	0.21 ± 0.04	1.2 ± 0.2	1.7 ± 0.3	3	3	0	3	1.3
00057	7.030	0.150	114 ± 11	0.21 ± 0.04	-1.0 ± 0.2	1.6 ± 0.3	9	9	0	0	1.4
00061	7.680	0.150	93 ± 9	0.17 ± 0.04	-1.0 ± 0.2	1.8 ± 0.3	10	10	0	0	1.3
00079	7.960	0.250	71 ± 7	0.23 ± 0.05	1.1 ± 0.2	1.3 ± 0.3	11	11	0	11	1.3
00103	7.660	0.150	87 ± 9	0.20 ± 0.045	-1.0 ± 0.2	1.6 ± 0.3	9	9	0	0	1.5
00119	8.420	0.150	65 ± 7	0.18 ± 0.04	1.2 ± 0.2	1.9 ± 0.4	10	10	0	10	1.6
00151	9.100	0.150	43 ± 4	0.22 ± 0.04	1.1 ± 0.2	1.4 ± 0.3	20	21	0	21	1.7
00158	9.270	0.150	44 ± 4	0.18 ± 0.04	1.3 ± 0.3	1.5 ± 0.3	15	15	15	15	1.7
00192	7.130	0.030	99 ± 10	0.25 ± 0.05	1.2 ± 0.2	1.5 ± 0.3	8	8	0	8	1.6
00192	7.130	0.030	99 ± 10	0.25 ± 0.05	1.2 ± 0.2	1.5 ± 0.3	6	6	0	5	1.6
00245	7.820	0.150	80 ± 8	0.21 ± 0.04	1.0 ± 0.2	1.6 ± 0.3	7	7	0	7	1.3
00288	9.840	0.150	33 ± 3	0.19 ± 0.04	0.9 ± 0.2	1.4 ± 0.3	9	10	11	11	1.3
00371	8.720	0.150	59 ± 6	0.17 ± 0.03	1.1 ± 0.2	1.7 ± 0.3	9	10	0	10	1.3
00532	5.810	0.260	193 ± 19	0.22 ± 0.05	-1.0 ± 0.2	1.1 ± 0.2	12	12	0	0	1.3
00584	8.710	0.240	54 ± 5	0.20 ± 0.04	1.0 ± 0.2	3.2 ± 0.7	5	4	0	6	1.6
00631	8.700	0.150	52 ± 5	0.22 ± 0.04	1.1 ± 0.2	1.4 ± 0.3	21	21	0	21	1.4
00699	11.720	0.150	13 ± 1	0.23 ± 0.05	1.0 ± 0.2	2.0 ± 0.4	4	0	8	8	1.2
00793	10.260	0.150	29 ± 3	0.16 ± 0.03	1.1 ± 0.2	1.7 ± 0.3	9	9	9	9	1.1
00793	10.260	0.150	29 ± 3	0.16 ± 0.03	1.1 ± 0.2	1.7 ± 0.3	13	13	13	13	1.1
00847	10.290	0.150	29 ± 3	0.16 ± 0.03	1.0 ± 0.2	1.6 ± 0.3	15	15	15	15	1.4
01036	9.450	0.300	36 ± 4	0.22 ± 0.04	1.0 ± 0.2	1.2 ± 0.3	9	9	9	9	1.3
01036	9.450	0.300	38 ± 4	0.20 ± 0.04	$1. \pm 0.2$	1.3 ± 0.3	13	13	13	13	1.3
01866	12.400	0.150	8 ± 1	0.29 ± 0.06	1.1 ± 0.2	1.3 ± 0.3	7	0	10	10	1.6
01980	13.920	0.150	5 ± 1	0.16 ± 0.03	1.4 ± 0.3	2.7 ± 0.5	5	0	7	6	1.7
01980	13.920	0.150	6 ± 1	0.15 ± 0.03	1.4 ± 0.3	2.1 ± 0.4	9	9	10	10	1.7
11500	18.400	0.150	0.8 ± 0.1	0.12 ± 0.02	1.6 ± 0.3	1.7 ± 0.3	10	20	20	20	1.4

Table 4. Best-fitting values of physical parameters determined for the Pallas Collisional Family asteroids excluding (2) Pallas with WISE observations. Negative values of η and or R_p indicate that the parameter was not free but fixed to the corresponding positive value. Errorbars shown are minimum estimates and correspond to 10% relative error for D , and 20% for η , p_V and R_p .

Designation	H	G	D [km]	p_V	η	R_p	W1	W2	W3	W4
00531	12.00	0.15	16 ± 2	0.10 ± 0.02	0.9 ± 0.2	-1.5 ± 0.3	0	8	12	12
03579	13.60	0.15	7 ± 1	0.12 ± 0.02	0.9 ± 0.2	0.4 ± 0.1	13	14	13	13
03579	13.60	0.15	7 ± 1	0.13 ± 0.03	1.0 ± 0.2	-1.5 ± 0.3	0	0	9	9
05222	11.30	0.15	19 ± 2	0.15 ± 0.03	1.0 ± 0.2	0.4 ± 0.1	13	13	13	13
05234	11.90	0.15	14 ± 1	0.15 ± 0.03	1.0 ± 0.2	-1.5 ± 0.3	0	0	6	6
05234	11.90	0.15	15 ± 2	0.13 ± 0.03	0.9 ± 0.2	-1.5 ± 0.3	0	0	10	10
05330	12.10	0.15	15 ± 2	0.11 ± 0.02	0.9 ± 0.2	0.6 ± 0.1	10	16	16	15
08009	13.70	0.15	6 ± 1	0.14 ± 0.03	1.3 ± 0.2	-1.5 ± 0.3	0	0	11	9
11064	12.60	0.15	9 ± 1	0.21 ± 0.04	1.2 ± 0.2	0.4 ± 0.1	16	17	17	17
12377	12.60	0.15	10 ± 1	0.15 ± 0.03	0.9 ± 0.2	-1.5 ± 0.3	0	0	9	9
14916	13.50	0.15	8 ± 1	0.12 ± 0.02	0.8 ± 0.2	-1.5 ± 0.3	0	0	8	9
15834	13.20	0.15	9 ± 1	0.11 ± 0.02	0.8 ± 0.2	-1.5 ± 0.3	0	0	9	9
23830	13.50	0.15	10 ± 1	0.07 ± 0.01	1.0 ± 0.2	-1.5 ± 0.3	0	5	12	12
24793	13.80	0.15	7 ± 1	0.11 ± 0.02	1.2 ± 0.2	-1.5 ± 0.3	0	0	12	12
24793	13.80	0.15	7 ± 1	0.13 ± 0.03	1.1 ± 0.2	-1.5 ± 0.3	0	10	13	13
25853	13.30	0.15	8 ± 1	0.14 ± 0.03	1.0 ± 0.2	-1.5 ± 0.3	0	0	6	6
33166	12.90	0.15	10 ± 1	0.12 ± 0.02	1.3 ± 0.2	-1.5 ± 0.3	0	0	14	14
33750	12.50	0.15	12 ± 1	0.12 ± 0.02	1.0 ± 0.2	0.6 ± 0.1	14	14	14	14
36273	12.80	0.15	9 ± 1	0.18 ± 0.04	1.0 ± 0.2	-1.5 ± 0.3	0	16	17	17
39646	13.50	0.15	4.4 ± 0.4	0.36 ± 0.07	0.8 ± 0.2	-1.5 ± 0.3	0	0	10	12
40101	14.10	0.15	6 ± 1	0.10 ± 0.02	1.4 ± 0.2	-1.5 ± 0.3	0	0	6	3
44232	13.10	0.15	9 ± 1	0.12 ± 0.02	1.1 ± 0.2	-1.5 ± 0.3	0	14	14	14
46037	13.70	0.15	6 ± 1	0.15 ± 0.03	1.1 ± 0.2	-1.5 ± 0.3	0	0	8	8
52229	13.60	0.15	8 ± 1	0.09 ± 0.02	1.0 ± 0.2	-1.5 ± 0.3	0	11	11	11
57050	13.50	0.15	7 ± 1	0.17 ± 0.03	0.8 ± 0.2	-1.5 ± 0.3	0	0	6	4
66714	14.30	0.15	6 ± 1	0.09 ± 0.02	1.1 ± 0.2	-1.5 ± 0.3	0	7	7	7
66714	14.30	0.15	5.5 ± 0.5	0.11 ± 0.02	1.2 ± 0.2	-1.5 ± 0.3	0	0	7	7
66803	12.50	0.15	8 ± 1	0.32 ± 0.06	1.0 ± 0.2	-1.5 ± 0.3	0	0	15	15
67370	13.70	0.15	6 ± 1	0.15 ± 0.03	1.0 ± 0.2	-1.5 ± 0.3	0	0	11	12
67779	12.60	0.15	10 ± 1	0.16 ± 0.03	0.9 ± 0.2	0.4 ± 0.1	11	13	13	13
69371	13.70	0.15	7 ± 1	0.11 ± 0.02	1.0 ± 0.2	-1.5 ± 0.3	0	0	21	20
69931	13.90	0.15	7 ± 1	0.11 ± 0.02	0.9 ± 0.2	-1.5 ± 0.3	0	12	12	12
82899	13.60	0.15	7 ± 1	0.13 ± 0.03	1.1 ± 0.2	-1.5 ± 0.3	0	0	11	11
87006	13.90	0.15	6 ± 1	0.14 ± 0.03	1.0 ± 0.2	-1.5 ± 0.3	0	7	9	9
90368	13.40	0.15	7 ± 1	0.14 ± 0.03	1.0 ± 0.2	-1.5 ± 0.3	0	0	8	8
A0590	14.60	0.15	5.1 ± 0.5	0.10 ± 0.02	1.2 ± 0.2	-1.5 ± 0.3	0	0	20	18
A1283	13.90	0.15	6 ± 1	0.15 ± 0.03	0.9 ± 0.2	-1.5 ± 0.3	0	0	7	7
A3779	14.40	0.15	3.9 ± 0.4	0.21 ± 0.04	-1.0 ± 0.2	-1.5 ± 0.3	0	0	8	0
A9640	13.70	0.15	8 ± 1	0.10 ± 0.02	1.1 ± 0.2	0.6 ± 0.1	17	21	21	21
B3770	14.10	0.15	6 ± 1	0.11 ± 0.02	1.0 ± 0.2	-1.5 ± 0.3	0	0	11	11

Table 4. continued.

Designation	H	G	D [km]	p_V	η	R_p	W1	W2	W3	W4
B8223	14.40	0.15	4.7 ± 0.5	0.14 ± 0.03	1.4 ± 0.2	-1.5 ± 0.3	0	0	13	12
C3349	14.70	0.15	4.1 ± 0.4	0.14 ± 0.03	1.2 ± 0.2	-1.5 ± 0.3	0	10	14	14
D6038	15.00	0.15	5.0 ± 0.5	0.07 ± 0.01	-1.0 ± 0.2	-1.5 ± 0.3	0	0	5	0
D8406	14.80	0.15	4.6 ± 0.5	0.10 ± 0.02	0.9 ± 0.2	-1.5 ± 0.3	0	0	9	8
E5861	14.60	0.15	4.5 ± 0.5	0.13 ± 0.03	-1.0 ± 0.2	-1.5 ± 0.3	0	0	3	0
F7914	14.10	0.15	7 ± 1	0.09 ± 0.02	1.2 ± 0.2	-1.5 ± 0.3	0	0	7	3
H6413	14.70	0.15	4.4 ± 0.4	0.12 ± 0.02	1.7 ± 0.2	-1.5 ± 0.3	0	0	7	5
I8324	14.50	0.15	6 ± 1	0.09 ± 0.02	1.3 ± 0.2	-1.5 ± 0.3	0	0	8	4
K6956	14.30	0.15	4.8 ± 0.5	0.15 ± 0.03	1.3 ± 0.2	-1.5 ± 0.3	0	0	4	3
N4076	14.20	0.15	4.7 ± 0.5	0.17 ± 0.03	-1.0 ± 0.2	-1.5 ± 0.3	0	0	4	0

Appendix A: Thermal modelling of WISE asteroid data

Our aim is to model the observed asteroid flux as a function of a number of physical parameters and derive the set of parameter values that most closely reproduce the actually measured fluxes. In this work we follow the method described by Mainzer et al. (2011b). The set of wavelengths covered by WISE (specified in Sect. 2) allow us to derive up to three parameters by fitting a thermal model to asteroid WISE data: asteroid effective diameter, beaming parameter and reflectance at $3.4 \mu\text{m}$ (defined below). Within the wavelength range covered, the observed asteroid flux consists of two components:

$$F_{\lambda}^{(m)} = f_{\text{th},\lambda} + r_{\text{s},\lambda}. \quad (\text{A.1})$$

The thermal flux component ($f_{\text{th},\lambda}$) is the main contribution to W3 and W4 whereas the reflected sunlight component ($r_{\text{s},\lambda}$) dominates in band W1. In general, W2 will have non-negligible contributions from both components (Mainzer et al. 2011b).

The computation of $f_{\text{th},\lambda}$ is based on the Near Earth Asteroid Thermal Model (NEATM; see Harris 1998; Delbó & Harris 2002). The asteroid is assumed to be spherical and its surface is divided into triangular facets which contribute to the total thermal flux observed by WISE in accordance to the facet temperature (T_i), the geocentric distance (Δ) and the phase angle (α_{\odot}). In turn, the temperature of each facet depends on the asteroid heliocentric distance (r_{\odot}) and its orientation with respect to the direction towards the sun. It is given by

$$\frac{S_{\odot}}{r_{\lambda}^2}(1 - A)\mu_i\delta a_i = \eta\sigma\epsilon T_i^4\delta a_i, \quad (\text{A.2})$$

which results from assuming that each surface element δa_i is in instantaneous equilibrium with solar radiation. S_{\odot} is the solar power at a distance of 1 AU, A is the bolometric Bond albedo, ϵ is the emissivity (usually taken to be 0.9; see

Delbó et al. 2007, and references therein), σ is the Stefan-Boltzmann constant and $\mu_i = \cos \theta_i$, where θ_i is the angle between the normal to the surface element i and the direction towards the sun. Non-illuminated facets will be instantaneously in equilibrium with the very low temperatures of the surroundings (~ 0 K) and thus their contribution to $f_{\text{th},\lambda}$ is neglected in the NEATM. Finally, the beaming parameter (η) can be thought of as a normalisation or calibration factor that accounts for the different effects that would change the apparent day-side temperature distribution of the asteroid compared to that of a perfectly smooth, non-rotating sphere (Harris 1998). These include, for example, the enhanced sunward thermal emission due to surface roughness ($\eta < 1$), or the non-negligible night-side emission of surfaces with high thermal inertia which, in order to conserve energy, causes the day-side temperature to be lower than that compared to the ideal case with zero thermal inertia ($\eta > 1$).

The asteroid thermal flux component is then given by

$$f_{\text{th},\lambda} = \Omega \sum_i f_{i,\lambda}(T_i), \quad (\text{A.3})$$

where $f_{i,\lambda}$ is the contribution from each illuminated facet of a 1-km sphere; $\Omega \equiv (D/1 \text{ km})^2$ scales the cross-section of the latter to the corresponding value of an asteroid of diameter D . The color correction associated with each value of T_i and each WISE band is applied to the facet flux. By definition, it is the quotient of the in-band flux of the black-body at the given temperature to that of Vega (Wright et al. 2010). A color correction table was generated for all integer temperatures from 70 K up to 1000 K using the filter profiles available from Cutri et al. (2012).

The reflected light component, the second term in the right hand side of Eq. A.1, is calculated as follows. First, the asteroid visible magnitude (V) that would be observed at a given ge-

ometry (r_\odot , Δ and α_\odot) can be estimated using the IAU phase curve correction (Bowell et al. 1989), along with the tabulated values of asteroid absolute magnitude (H) and slope parameter (G) from the Minor Planet Center. Secondly, knowledge of the solar visible magnitude and flux at $0.55 \mu\text{m}$ (V_\odot and f_{V_\odot} , respectively) allows us to calculate the sunlight reflected from the asteroid at that particular wavelength:

$$r_V = f_{V_\odot} \times 10^{-\frac{V-V_\odot}{2.5}}. \quad (\text{A.4})$$

If we assume that the sun is well approximated by a black body emitter at the solar effective temperature ($T_\odot = 5778 \text{ K}$), the estimated reflected flux at any other desired wavelength (r_λ) can be computed by normalising the black body emission $B_\lambda(T_\odot)$ to verify r_V , i.e.

$$r_\lambda = r_V \frac{B_\lambda(T_\odot)}{B_V(T_\odot)}. \quad (\text{A.5})$$

In this approximation, we can also consider

$$\frac{B_{IR}(T_\odot)}{B_V(T_\odot)} \approx \frac{f_{IR_\odot}}{f_{V_\odot}}, \quad (\text{A.6})$$

from which we arrive at the following expression:

$$r_\lambda = f_{IR_\odot} \frac{B_\lambda(T_\odot)}{B_{IR}(T_\odot)} \times 10^{-\frac{V-V_\odot}{2.5}}, \quad (\text{A.7})$$

where the subscript IR denotes $3.4 \mu\text{m}$. Note that we do not color correct this component given the small correction to the flux of a G2V star (see Table 1 of Wright et al. 2010). Finally, in order to account for possible differences in the reflectivity at wavelengths longward of $0.55 \mu\text{m}$, a prefactor to r_λ is included in the model, such that

$$r_{s,\lambda} = R_p r_\lambda. \quad (\text{A.8})$$

This prefactor, R_p , is by definition equivalent to the ratio of p_{IR} and the the visible geometric albedo, so we will refer to it as the ‘‘albedo ratio’’. The parameter p_{IR} is the reflectivity at 3.4 and $4.6 \mu\text{m}$ defined by Mainzer et al. (2011b).

To sum up, the observed model flux can then be written as:

$$F_\lambda^{(m)} = \Omega \sum_i f_{i,\lambda} [T_i(\eta)] + R_p r_\lambda. \quad (\text{A.9})$$

We use the Levenberg-Marquardt algorithm (Press et al. 1986) in order to find the values of asteroid size ($D = \sqrt{\Omega}$, in km), beaming parameter (η) and albedo ratio (R_p) that minimise the χ^2 of the asteroid’s WISE data set, namely

$$\chi^2 = \sum_{j,\lambda} \left(\frac{F_{j,\lambda} - F_{j,\lambda}^{(m)}}{\sigma_{j,\lambda}} \right)^2, \quad (\text{A.10})$$

where $F_{j,\lambda}$ and $\sigma_{j,\lambda}$ are the measured fluxes and corresponding uncertainties, j runs over the observation epochs and λ labels the WISE bands. The implementation of this technique involves the calculation of the partial derivatives of $F_\lambda^{(m)}$ with respect to the fitting parameters, which is straightforward in the case of Ω and R_p . The partial derivative with respect to η can be derived from:

$$\frac{\partial F_\lambda^{(m)}}{\partial \eta} = \left(\frac{\partial F_\lambda^{(m)}}{\partial T_i} \right) \left(\frac{\partial T_i}{\partial \eta} \right). \quad (\text{A.11})$$

The derivation of the exact analytical expression for the first factor is considerably long to be included here, whereas the derivative of T_i with respect to η is easily obtained from Eq. A.2.

Appendix B: Comparison with Masiero et al. (2011)

Figure 2 shows that our parameter determinations and those of Masiero et al. (2011) are compatible in spite of the slight differences in the data set and the thermal modeling used in this work (refer to Sect. 2 and Appendix A), from which we do not expect to obtain exactly the same best-fit parameters for each object. In order to carry out a detailed comparison between our results and those of Masiero et al. (2011), we computed the mean fractional difference (ε) and corresponding standard deviations of D , η , p_V and R_p . Let $\varepsilon = 100(x - x_M)/x$, where x is the parameter value for a given object in this work and x_M is the corresponding value taken from Table 1 by Masiero et al. (2011). The distributions of ε values are plotted in Fig.

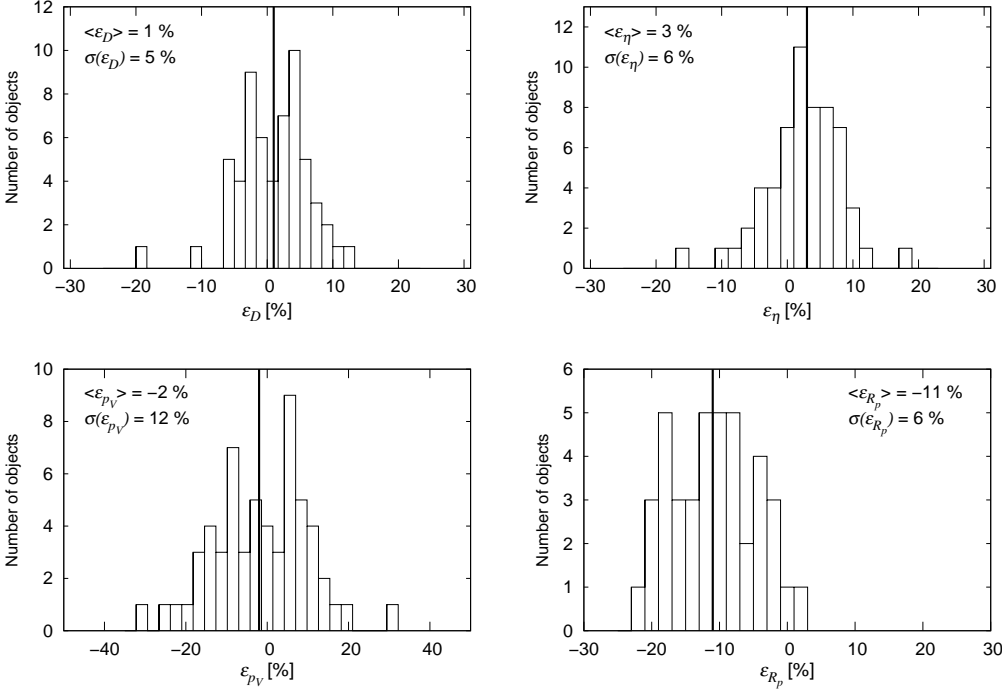


Fig. B.1. Fractional difference histograms of D , η , p_V and R_p . We define $\varepsilon = 100(x - x_M)/x$, where x is the parameter value in this work and x_M is the corresponding value taken from Table 1 by Masiero et al. (2011). The vertical lines mark the corresponding average values. Note: only parameters resulting from the same input values of H contribute to these histograms.

B.1. These histograms only include parameter determinations that have the same H as input in order to identify possible discrepancies in results not caused by different values of H . We find that our values of D and η tend to be slightly greater by 1% and 3%, respectively, whereas our p_V values are lower by 2%, though these deviations are small compared to the errorbars. On the other hand, there is a large bias towards lower values of R_p that, while still being within the errorbar, must be addressed.

Most probably, the R_p discrepancy is associated with how the reflected flux r_λ is calculated. In particular, we take the solar flux at $3.4 \mu\text{m}$ (f_{IR_0} in Eq. A.7) from the solar power spectrum at zero air mass of Wehrli⁴, based on that by Neckel & Labs (1984). Any differences in input, including solar visible magnitude, taken from tabulated data sources that may cause our

r_λ to be systematically 10% greater than that of Masiero et al. (2011) would explain our higher values of R_p . For instance, taking into account that there is only one optimum value of $r_{s,\lambda}$ to fit a given W1 data set, from Eq. A.8 it is clear that a larger r_λ will have associated a lower best-fit value of R_p .

The Monte Carlo estimations by the NEOWISE team show that the errorbars associated to the fitting of the data are always small compared to the errors inherent to the thermal model itself. The relative errors in diameters derived from the NEATM have been characterised to be $\sim 10\%–15\%$ (Harris 2006). From these facts and the widths of the ε -value distributions of Fig. B.1, we consider it safe to assume a minimum relative error of 10% in diameter and 20% in beaming parameter, p_V and R_p . On the other hand, large uncertainties in the absolute magnitude (sometimes as large as ~ 0.3 magnitudes)

⁴ <http://trcdc.nrel.gov/solar/spectra/am0/wehrli1985.new.html>

will also affect the values of p_V , so 20% is probably an optimistic assumption in some cases.

Finally, we also evaluate how differences in the values of H result in different values of p_V and R_p . We downloaded the MPC orbital element file as of May 2012 and compared the values of absolute magnitude (H_U) to those used by Masiero et al. (2011), H_M . About 50000 H -values have been updated between these two works, and ~ 38000 have been enlarged. Figure 1 shows a histogram of $\Delta H \equiv H_U - H_M$ for the B-types in this work. Out of the 52 objects with $\Delta H \neq 0$, as many as 43 of them have $\Delta H > 0$. Our size determinations agree to within 10%, therefore larger updated values of H will result in lower values of geometric albedos.

In Fig. B.2 we show a plot of $\Delta R_p \equiv R_p - (R_p)_M$ versus ΔH for all the B-types with determined values of R_p . The notation $(R_p)_M$ refers to the corresponding albedo ratios by Masiero et al. (2011). There are three features to note in this plot: (1) our values of R_p tend to be $\sim 10\%$ systematically lower, as we already noted (see Fig. B.1); (2) most points off the $\Delta H = 0$ axis show a direct correlation between ΔR_p and ΔH , as expected from the discussion above; (3) some points show $\Delta R_p < -0.5$ even though $\Delta H = 0$. The points of feature (3) are explained by an inconsistency in the p_V values of Masiero et al. (2011) with their corresponding values of D and H : they do not verify Eq. 1 and are always lower than the predicted p_V .

To sum up, we have shown that if the input values of H are equal, our model fits are consistent within the model errorbars with those presented in Table 1 of Masiero et al. (2011). The tendency to 10%-lower values of R_p is likely caused by differences in solar power spectra data taken to estimate the reflected light component at NIR wavelengths (see Eq. A.7). We have also examined how updated input values of H affect the best-fit parameter values and showed

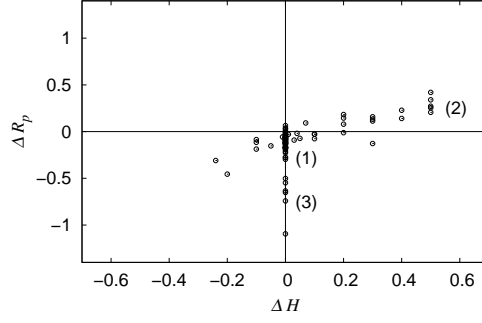


Fig. B.2. Differences in albedo ratio determinations versus difference in absolute magnitude corresponding to the B-types in this paper and those by Masiero et al. (2011). Note that while the majority of cases verify $\Delta H = 0$, our R_p values tend to be lower (1). On the other hand, some of the differences in albedo ratio (2) are explained by the differences in the updated values of H used in this paper. Finally, some points show very large differences, $\Delta R_p < -0.5$, in the albedo ratio value (3) despite the fact that $\Delta H = 0$ (more details in the text).

how increasing the value of H results in greater values of R_p and vice versa.